**FACULTY
OF MATHEMATICS
AND PHYSICS**
Charles University

MASTER THESIS

Daniel Staško

Pressure effects on physical properties of a selected Ce-based compound

Department of Condensed Matter Physics

Supervisor of the master thesis: RNDr. Milan Klicpera, PhD.

Study programme: Physics

Specialization: Physics of Condensed Matter and Materials

Prague 2020

I declare that I carried out this master thesis independently, and only with the cited sources, literature and other professional sources.

I understand that my work relates to the rights and obligations under the Act No. 121/2000 Coll., the Copyright Act, as amended, in particular the fact that the Charles University has the right to conclude a license agreement on the use of this work as a school work pursuant to Section 60 paragraph 1 of the Copyright Act.

In…....... date............   signature

Title: Pressure effects on physical properties of a selected Ce-based compound

Author: Daniel Staško

Department: Department of Condensed Matter Physics

Supervisor of the master thesis: RNDr. Milan Klicpera, PhD., Department of Condensed Matter Physics

Abstract: Presented thesis focuses on the study of transport properties of two intermetallic compounds, $CeRhSi_3$ and $CeCuAl_3$, under high external pressure. High-pressure dependence of previously reported pressure induced superconductivity in $CeRhSi_3$ is studied closely up to 4.6 GPa, focusing on the, so-far-unstudied, pressure region above 3 GPa. After reaching maximal value at 2.9 GPa, the critical temperature of superconducting transition is gradually suppressed by further pressure application. Extensive search for possible pressure induced superconductivity in $CeCuAl_3$ is conducted, employing solid-pressure-medium Bridgman anvil cells with theoretical pressure limit of 12 GPa. No pressure induced superconductivity is observed up to 4.5 GPa and down to 8 mK. Additionally, a calibration study of three liquid pressure exchange media from Daphne Oil 7000 series is carried out in order to advance high pressure experimental techniques. Comprehensive results about hydrostaticity, solidification, pressure drop and compressibility of individual pressure media are presented.

Keywords: $CeCuAl_3$, high pressure, noncentrosymmetric compounds, vibron states, superconductivity

Contents

Introduction

Ce-based intermetallic compounds frequently exhibit interesting magnetic and transport properties originating in a partially filled 4f-level, and therefore remain of interest of the condensed matter physics community. A family of $CeTX_3$ (T – transition d-metal, X – p-metal) intermetallic compounds exhibit a variety of frequently exotic properties, such as valence fluctuations, heavy fermion antiferromagnetic ordering, pressure induced superconductivity or the so called vibron quasi-bound state [1,2,3,4]. Also the pressure induced superconductivity emerging in non-centrosymmetric Ce-based compounds attracted a significant interest in recent years [2,3,5].

Application of high external pressure is at present one of the most experimentally challenging techniques employed in the condensed matter research, considerably more challenging than variation of temperature and magnetic field. Nevertheless, it represents a unique way of clean and direct variation of interatomic distances in the crystallographic lattice, being thus an important tool in the study of intricate electron structure of rare earth intermetallics.

Presented study focuses firstly on high pressure measurements of transport properties of $CeRhSi_3$ and $CeCuAl_3$ compounds, crystallizing in the tetragonal non-centrosymmetric ordered structure. Pressure induced superconductivity reported in $CeRhSi_3$ is studied in yet unexplored pressure region up to 4.6 GPa. A search for pressure induced superconductivity in $CeCuAl_3$ is conducted under extreme conditions. Second focus of presented work is directed at the characterization of high pressure exchange media, specifically the calibration of three liquid media from the Daphne Oil 7000 series.

Presented thesis consists of: Theoretical information relevant to proposed study in chapter 1. Theory. Description of used experimental techniques emphasizing the pressure experiments in chapter 2. Experimental methods. Previous results on $CeRhSi_3$ and $CeCuAl_3$ in chapter 3. Previous results. Experimental data accumulated during the study in chapter 4. Results and discussion of those results in chapter 5. Discussion form the main part of the thesis. Obtained results are summarized in Conclusions.

1. Theory

1.1. External Pressure

Pressure is one of the basic thermodynamic parameters. Alongside temperature and magnetic field, it is an important variable in the study of material properties. Upon the application of external pressure, the interatomic distances in the elementary unit cell begin to change; individual distances may decrease or increase, while the unit cell volume always decreases. There are 3 standard methods of changing the interatomic distances and each of them have their own characteristics. Chemical substitution (or chemical pressure) changes interatomic distances by replacing a (small) percentage of atoms in parent compound by different element(s). Chemical doping, however, results in different electron configuration as the material has different number of electrons due to the substituted atoms. Temperature variation does not affect the chemical structure (setting aside changes of crystal structure and corresponding symmetries), nevertheless it can lead to the changes of the occupation numbers of the quantum states. Applying external pressure is a clean way of changing the interatomic distances which results in a variation in energy of the quantum states [6].

Pressure is generally defined as the force, F, applied on an area S

$$p = \frac{F}{S},\tag{1}$$

or as an energy density

$$p = \left(\frac{\partial F_H}{\partial V} \right)_T,\tag{2}$$

where F_H is a Helmholtz free energy. The applied force is often a vector, and the surface can be perpendicular to any of its three directions. Therefore, it is necessary to recognize different components responsible for the stress in a material. These can be accounted for with the use of the so-called stress tensor defined as

$$\sigma = \begin{pmatrix} \sigma_{11} & \sigma_{12} & \sigma_{13} \\ \sigma_{21} & \sigma_{22} & \sigma_{23} \\ \sigma_{31} & \sigma_{32} & \sigma_{33} \end{pmatrix}.\tag{3}$$
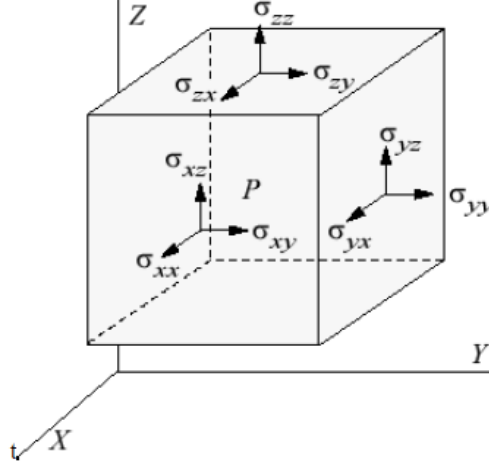
Fig.1: Stress tensor components. Image taken from [6].

9 components of the stress tensor (see illustrative image in Fig.1) can be split into 3 diagonal ones, σ_{ii}, representing direct stress and 6 non-diagonal components, σ_{ij} ($i \neq j$), standing for shear stress. A direct stress is always normal to the surface of the material exposed to the external pressure and governs a change of its volume. The response of the material to the stress is characterized by material compressibility or its inverted function - the bulk modulus. 6 remaining components stand for a shear stress tangential to the surface; 2 components for each orthogonal surface. The shear stress deforms the material, i.e. changes the shape of the material without the change of its volume. All of these components are defined at each point of space (imagine an infinitesimally small cube) in a certain time, which lead us to a definition of pressure as [6]

$$p(r,t) = -1/3 \left(\sigma_{11} + \sigma_{22} + \sigma_{33} \right).$$
(4)

Similarly, the shear stresses can be described with the deviatoric stress tensor as

$$\Delta(r,t)_{ij} = \sigma(r,t)_{ij} - \delta_{ij}\, p(r,t).$$
(5)

High pressure experiments generally tend to focus on 2 types of pressure conditions: hydrostatic and uniaxial. An ideally hydrostatic pressure applied on the material causes a decrease of sample volume, while no deformation of the sample shape (or its destruction) is induced. Hydrostatic conditions are obtained by surrounding the sample by a co-called pressure exchange medium, which equally redistributes the pressure within the sample space (more in the section 2.3.3. High pressure media). It can be defined as a pressure with zero deviatoric shear stress and isotropic normal stresses [6]:

$$p(r,t) = -\sigma_{11}(r,t) = -\sigma_{22}(r,t) = -\sigma_{33}(r,t), \qquad \Delta(r,t)_{ij} = 0. \qquad (6)$$

Uniaxial pressure has only one normal stress component non-zero. This usually results in a compression of the sample along the specified direction accompanied by an expansion in the perpendicular directions. Uniaxial experiments are therefore very sensitive to a correct plane-parallel apparatus and are prone to sample destruction in the process. However, the ability to control interatomic distances in one particular direction comes forth with the study of oriented single crystals, as it is a unique tool for attuning specific structural and electronic properties.

Many experiments striving for ideal hydrostatic pressure conditions are limited by the non-hydrostatic tendencies at high pressures. There exists a so called quasi-hydrostatic condition, typically associated with anvil pressure cells and a pressure medium in the solid state. The pressure, while locally hydrostatic, has a different value in different positions of the sample space. Experimental pressure distribution can be approximated with a calculation of pressure distribution of "dry" contact of two bodies, which can be analytically expressed as [7]

$$p_\lambda(r) = \frac{2\lambda+1}{2} \frac{Q}{\pi a^2} \int_0^{\sqrt{1-r^2/a^2}} \left(\frac{r^2}{a^2} + x^2\right)^{\lambda-1} dx, \qquad (7)$$

where Q is the applied load, a is the radius of the contact area and λ describes the shape of the indenter. See Fig.2 with calculated distribution of pressure for cone, sphere and cylinder. Although it is important to consider the effect of bevelled anvil as well as the presence of a gasket, numerous authors observed a nearly conical distribution for flat anvils [7].
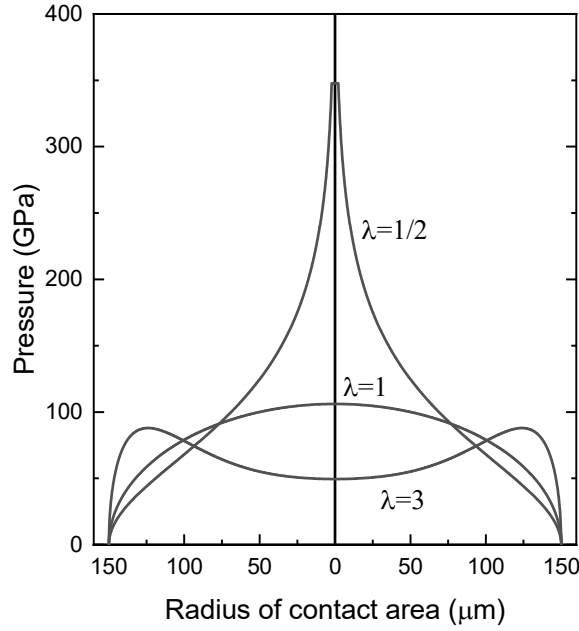
Fig.2: Pressure redistribution over the area of elastic contact of cone (λ=1/2), sphere (λ=1) and near cylinder (λ=3) indenter with a plane calculated with (7). Calculations were made with the same contact area $a=150\,\mu m$ and load $Q=250\,kg$ [7].

Comparing the application of external pressure on the sample to a variation of temperature or magnetic field, the former is significantly more experimentally and technically challenging. The main issues with applying the pressure to influence material properties are frequently connected with a necessity to combine the pressure with temperature or/and magnetic field variation, i.e. rather limited dimensions of sample space, high demands for pressure cell material from the viewpoint of durability, thermal conductivity and magnetic properties. Of course, further demands on pressure cells properties are dictated by specific experimental techniques, e.g. a transparency for X-ray diffraction experiments, or low cell-material absorption cross-section for neutron scattering experiments.

1.2. Electrical resistivity

Electrons in metal behave in accordance with the Ohm's law based on the electrical field and the conductivity of the material [8]

$$\vec{j}=\sigma\,\vec{E}. \tag{8}$$

A simple relation of electrical conductivity σ can be obtained in the Fermi gas model, as well as the electrical resistivity ρ defined as the reciprocal of the conductivity [8]

$$\sigma = \frac{ne^2\tau}{m_e} , \tag{9}$$

$$\rho = \frac{m_e}{ne^2\tau} , \tag{10}$$

where n is a number of electrons per unit volume, τ is the collision time, and m_e and e are the mass and charge of an electron, respectively. The electrons moving within the sample are scattered by several mechanisms. Considering the individual mechanisms are independent, the total electrical resistivity can be written as a sum of its contributions. Matthiessen's rule is hence written as

$$\rho = \rho_0 + \rho_{phonon} + \rho_{mag} + \dots . \tag{11}$$

We restrict ourselves to a brief description of the most general contributions to the electrical resistivity. The conduction electrons collide with various imperfections in the crystal structure, be it impurities or various other defects of the lattice. This so-called residual resistivity contribution, ρ_0, is generally independent on temperature, since the concentration of defects in the sample remains the same (not considering extreme conditions, e.g. temperature close to the melting temperature). Therefore, it is most pronounced at low temperature where a majority of other contributions exhibits the lowest values.

Further, the electrons scatter on phonons (lattice vibrational modes) which are highly dependent on temperature and can be described by the Bloch-Grüneisen function as [9]

$$\rho_{phonon} = K\left(\frac{T}{\theta_D}\right)^5 \int_0^{\theta_D/T} \frac{x^5}{(e^x-1)(1-e^{-x})} dx , \tag{12}$$

where K is a material constant and θ_D is a Debye's temperature. The phonon contribution behaves linearly at high temperatures and decreases rapidly ($\sim T^5$) at low temperatures.

The magnetic contribution, ρ_{mag}, results from an interactions between conduction electrons and uncompensated magnetic spins of material electrons. In a paramagnetic state of the material, ρ_{mag} is constant, because the magnetic moments are randomly oriented independent of temperature. Below magnetic ordering temperature, the moments become aligned and their precession is governed by further decreasing temperature. Therefore, the resistivity decreases in the ordered state with decreasing temperature. The transition from paramagnetic to ordered state is generally pronounced as a kink in the resistivity data as depicted in Fig.3.
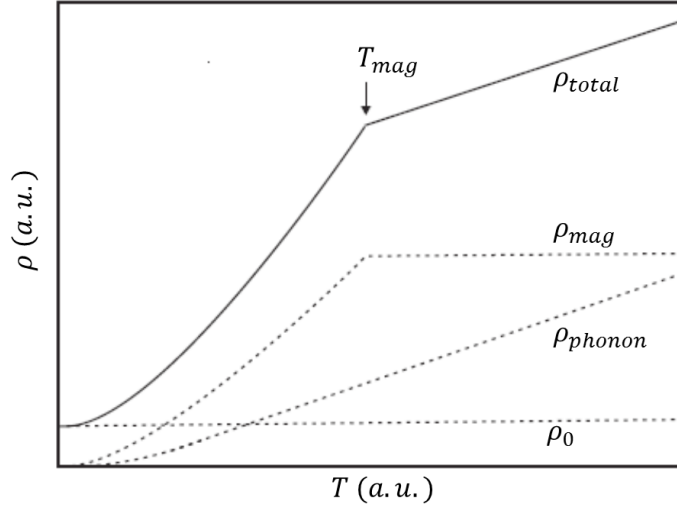
Fig.3: Illustration of the electrical resistivity contributions in a magnetic material with an ordering temperature T_{mag} [10].

1.3. Pressure effects on superconductivity

Superconductivity (SC) was first observed in 1911 by H. Kamerlingh Onnes, when the resistivity of Hg suddenly dropped to zero at 4.19 K. Following this discovery, SC was studied in a number of pure elements at ambient pressure and later under external pressure - in materials, which are non-SC at ambient pressure.

To approximate how pressure affects superconducting transition temperature, T_c, which is a necessity conducting any pressure experiment, the microscopic theories of phonon mediated SC, e.g. the weak-coupling BCS model, are to be considered. According to BCS model, T_c is influenced by the average phonon frequency ω_D, the electronic density of states at Fermi level $N(E_F)$ and the effective interaction between the electrons mediated by the electron-phonon coupling V_{eff} as follows [11]

$$k_B T_c = 1.13 \hbar\, \omega_D \exp\left(-1/N\left(E_F\right) V_{eff}\right), \tag{13}$$

within the weak-coupling condition $k_B T_c \ll \hbar\omega$. Phonon frequency tends to increase under pressure (the so-called phonon hardening), which leads to an increase of T_c. However, the density of states is affected by pressure as well. The overlap of electron orbitals leads to a broadening of electron bands, resulting in a decrease of $N(E_F)$ and according to (13) also T_c. To estimate a development of V_{eff} is even more challenging. T_c for ambient pressure superconductors decreases with increasing pressure as evidenced by empirical studies [11]. In contrast, T_c of pressure induced SC has a

tendency to initially increase, reach a maximum and then decrease, ultimately disappearing (the so called dome behaviour) [11].

1.4. Crystal electric field

Unlike the case of an isolated ion, in the crystal lattice the ion with non-zero magnetic moment is surrounded by other (non-magnetic) ions, which create the electric field acting on it. The crystal electric field (CEF) acting on magnetic ion has a symmetry specified by the local crystallographic environment and strength dictated by individual ions (charges) within the lattice. CEF plays a crucial role in the formation of electronic properties of compounds with magnetic ions being transition d-metals, 4f rare-earth elements and 5f actinides. In 3d-metals based compounds, CEF is stronger than spin-orbit (SO) coupling. In rare-earths materials, SO coupling prevails and CEF can be considered as a perturbation, influencing the lowest J multiplet.

A good example of a rare-earth ground state multiplet CEF splitting is demonstrated on Ce-based intermetallic compounds. The degeneracy of the ground state multiplet ($J=5/2$; $2J+1=6$ levels) of Ce^{3+} ion is removed in the crystal environment. Considering the Kramers´ theorem on J being half integer, the CEF splits the ground state multiplet into either one doublet and one quadruplet in the case of cubic environment, or into three doublets. The energies of individual levels (eigenenergies of CEF Hamiltonian, as well as CEF parameters) are standardly measured by inelastic neutron scattering, however they mirror themselves also in macroscopic properties of the studied material, e.g. magnetization, specific heat and electrical resistivity.

2. Experimental methods

The majority of devices employed in the presented study for sample preparation, characterization and transport properties measurements are available at the Department of Condensed Matter Physics (DCMP) and are part of Material Growth and Measurement Laboratory (MGML) [12].

2.1. Sample preparation

Single crystal samples were prepared by two methods: Czochralski pulling method in a tri-arc furnace and the flux growth method [12].

2.1.1. Mono-arc furnace

First step in the preparation of the single crystals is generally the preparation of poly-crystalline precursors. The polycrystal can be prepared by various methods. One of the simplest method is a direct arc-melting of the conductive elements in the mono-arc furnace. High purity elements, Ce of 99.8% (2N8) purity with additional purification by in-house SSE, Cu 6N, Al 6N, Rh 3N5 and Si 6N, were used for the sample preparation. High purity Ce tends to react with oxygen over time, therefore it is preserved in an argon atmosphere in the glove box [12]. Before melting, each element is carefully weighed to achieve correct stoichiometry of the final compound. Heat used for the melting of the elements is produced by arc discharge between two electrodes – one sharp manually movable W electrode and the second one being a Cu plate with multiple small bowls. Both electrodes are water cooled. Preparing the sample, first the interior of the mono-arc furnace is evacuated down to 10^{-4} Pa and simultaneously heated up to about 80°C. Subsequently, the chamber is filled with argon of 6N purity. Finally, the elements are melted by arc. It is advisable to put heavier elements (with higher melting temperature) atop of lighter ones to improve the mixing process during the melting. Prepared polycrystal is repeatedly turned around and re-melted to achieve a good homogeneity of the sample.

2.1.2. Tri-arc furnace/ the Czochralski method

Tri-arc furnace is constructed for the growth of single-crystalline samples employing the Czochralski method. Similarly to mono-arc furnace, the chamber is evacuated and subsequently filled with high purity argon atmosphere during the crystal growth.

The basic idea is to slowly pull a W rod (or a rod with a crystal seed) out of a molten polycrystalline sample prepared beforehand in the mono-arc furnace. W is a preferable material because of its high melting point, which reduces a chance of adding impurities to the sample. Molten polycrystalline sample is held in a Cu crucible with its temperature controlled by the current of three electrodes placed evenly around the sample. Both the seed rod and the crucible counter-rotate during the preparation process and they are both constantly cooled. The speed of the rod pulling the ingot as well as the rotation speed are different for individual materials. By carefully altering the current in the electrodes, it is possible to change the diameter of the growing crystal, e.g. high current (and therefore high temperature) results in the decrease of the crystal diameter, because the rod cooling cannot keep up. It is typical to decrease the diameter to the smallest possible and then widen it in order to create the so-called "neck". By doing so, there is a higher probability of only one crystalline grain surviving and propagating along the ingot. The final product is ideally a single-crystalline sample typically a few cm long and a few mm in diameter. The image of the inner space of tri-arc furnace together with prepared CeRhSi$_3$ ingot is presented in Fig.4.
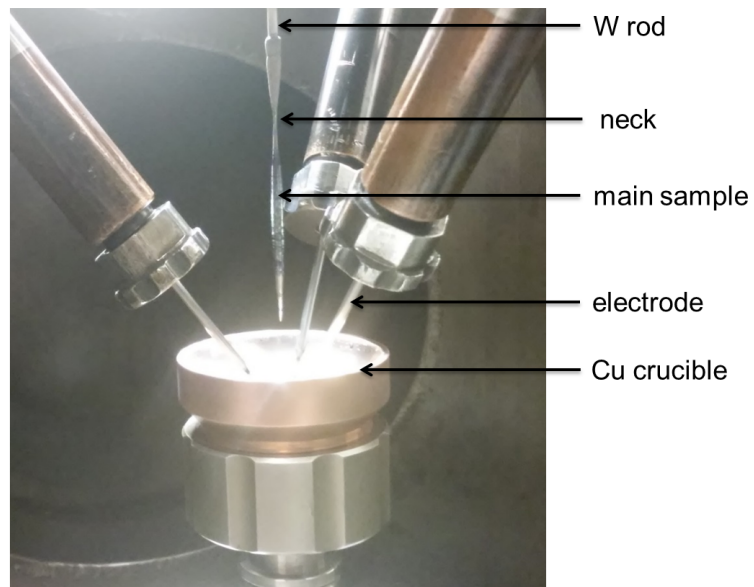

Fig.4: Single crystal growth by Czochralski pulling method in the tri-arc furnace [12]. The ingot is attempted CeRhSi$_3$ sample (see also section 4.1.1. Sample preparation and characterization).

2.1.3 Flux growth method

The solution (flux) growth method is used for producing small single crystals of very high quality. In principle, the desired sample composition – solute and the flux material – solvent, together create a solution. Such a solution enables a slow growth of the desired sample (single crystal) at temperatures lower than the melting temperature of the desired solute phase. Ideally, small single crystals grow naturally from nucleation, typically forming facets in various crystallographic directions. There are two types of flux growth methods: self-flux, in which the solvent (flux) is part of the compound composition and true-flux, in which the flux is a different element from the ones in the desired compound. Firstly, all components and the flux are put in a crucible (typically made of sintered Al_2O_3 or high-temperature resistant elements e.g. Ta, Pt) and evacuated in a quartz tube. Sealed tube is subsequently inserted into resistance furnace and heated to a temperature needed to create a homogenous liquid. After proper homogenization, temperature is decreased very slowly to allow crystal growth. Final step of preparation consists of quick separation of grown crystals from the flux, e.g. by centrifugation through quartz wool, which can be inserted on the other side of the crucible at the beginning of the whole preparation process. For the growth of $CeRhSi_3$ single crystals, Sn flux was used.

2.2. Sample characterization

Sample characterization was done employing three methods: Laue X-ray diffraction for determination of quality and orientation of the prepared single crystals, powder X-ray diffraction for crystal structure and sample phase purity confirmation and energy-dispersive X-ray spectroscopy (EDX) for composition and phase homogeneity analysis.

2.2.1. Laue X-ray diffraction

The Laue X-ray diffraction method can be used to quickly, easily and non-destructively gain some basic information about a single crystalline sample, i.e. information about its symmetry, orientation and overall quality/phase-homogeneity. A polychromatic X-ray beam is diffracted on a single crystalline sample and detected by X-ray detector located behind the sample (transmission Laue method) or between the X-ray source and the sample (back-reflection Laue). High quality single crystal causes that the diffracted radiation create singular sharp spots on the detector. These

spots represent reflections for each indexed crystallographic plane. Diffraction on the sample consisting multiple phases (several crystal grains with either the same or different crystal structure) results in multiple reflections, which, of course, cannot be described by single model structure. Ultimately, concentric circles are formed in the case of a polycrystalline sample. Large quantity of defects in the structure leads to smeared spots. In the case of back-reflection geometry (employed in this study), spots on the detector form hyperbolae; all reflections on a single hyperbola belong to crystallographic planes from one zone [13]. For tetragonal structure (the crystal structure of investigated compounds, see section 3.1. Crystal structure), Laue diffractogram showing 4-fold symmetry immediately identifies the crystallographic c direction (direction [001] or equivalently plane (001)), making the sample orientation process straightforward. Here, we highlight that the technique is mainly surface sensitive; a little information on the bulk can be derived from laboratory X-ray Lauegram. To properly verify the quality of the single crystal, the scans on different places of the sample, including rotation of the sample by 180 degrees, are essential. We used Laue X-ray diffractometer PhotonicScience [12].

2.2.2. Powder diffraction

X-ray powder diffraction is a widely spread method used mainly for the determination of crystal structure, phase purity and lattice parameters. In simple terms, the intensity of diffracted X-ray beam is detected depending on the diffraction angle. Resulting diffraction patterns contain peaks (of different intensity), corresponding to the crystal structure symmetry and lattice parameters. Many complex variations of this method exist (capable of studying preferred grain orientation, internal stresses etc.) [13], but for a standard characterization of prepared samples, we restrict ourselves to use the symmetrical Bragg-Brentano option. In such a setup, X-ray radiation is diffracted on planes which are parallel to the scattering plane for a given 2θ angle. If the structure of the material is known, powder diffraction can determine the phase purity of the sample, i.e. in case of phase pure sample, all measured peaks are described by single crystal structure model, which free parameters can be refined. For the analysis of the diffraction patterns, the FullProf package using the Rietveld method was used [14]. Device used for the powder diffraction experiment was powder diffractometer Bruker D8 Advanced (see Fig.5).
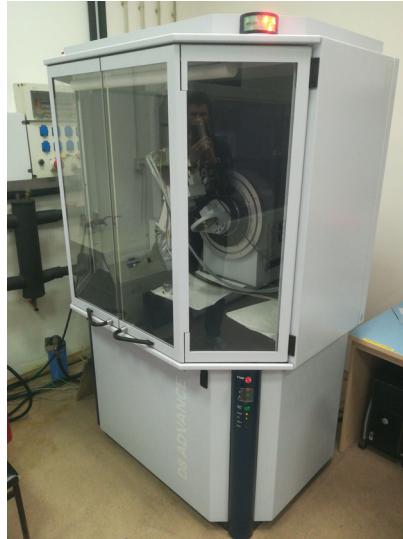
Fig.5: X-ray powder diffractometer Bruker D8 Advanced [12].

2.2.3. Scanning electron microscopy

With a use of scanning electron microscope (SEM), information such as surface topology and composition of the sample can be obtained. In SEM, a conducting grounded sample with evacuated surroundings is exposed to a focused electron beam of adjustable energy. Detection of secondary electrons results in a clear topological image of the surface. Detection of back-scattered electrons (BSE) gives not just topological information, but can also distinguish between concentrations of lighter/heavier atoms (electrons are more likely back-scattered on heavier nuclei, resulting in higher intensities detected and thus brighter image in the area of high concentration of heavy atoms). Lastly, inelastic electron scattering can result in an excitation of core electrons in the atoms. The emptied energy levels (orbitals) are occupied by electrons from higher energy levels, and X-ray radiation, corresponding to the difference between energies of the two levels, is detected (principle of EDX – energy dispersive X-ray analysis). The energy spectrum of the element is called characteristic, as it is different for individual elements, and enables the EDX technique to determine the composition of the (surface of the) sample. Although EDX is more qualitative than quantitative method, it can be used to map the sample surface and refer on its stoichiometry, homogeneity of elements distribution and phase purity. In this study, TESCAN Mira I LMH microscope was used [12].

2.3. High pressure techniques

High pressure experiments remain to be some of the most experimentally challenging techniques in the field of condensed matter study. Pressure is commonly applied in specialized pressure cells of various design, accompanied by different pressure determination techniques and pressure exchange media. In this study, 3 different pressure cells were used.

2.3.1. Bridgman anvil cells

Bridgman anvil cells (BAC) are named after their inventor Percy Williams Bridgman, who was given a Nobel Prize in 1946 for their invention and experimental accomplishments. They are essentially the predecessors of diamond anvil cells (DAC), which work almost the same in principle. As shown in Fig.6, the pressure is applied by forcing two plane-parallel anvils against each other reducing the space between them. The sample space is supported by a circular gasket. Anvils are made of especially hard materials, but unlike the anvils in DACs, there are not transparent. We used anvils made of WC (tungsten carbide) and PkDia (type of artificially manufactured diamond). Over the years, various modifications were made on the standard BAC for the purpose of e.g. the use of different types of pressure media or different arrangement of contact wires. We used two types of BAC.
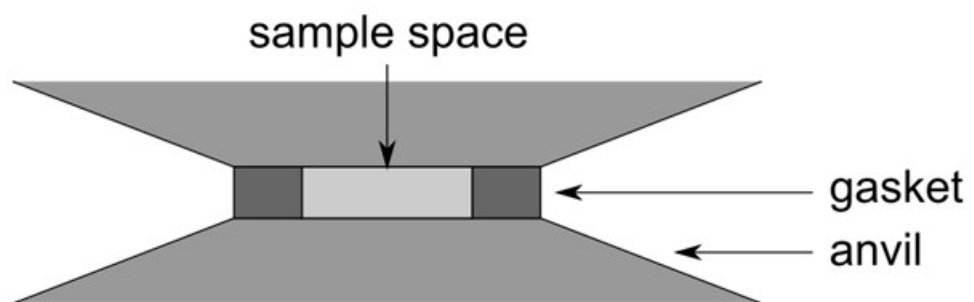
Fig.6: Basic scheme of a Bridgman anvil cell.

First type is a modified BAC for the use of liquid pressure medium – l-BAC. Contrary to solid pressure media frequently used in BACs, liquid ones generally provide more hydrostatic conditions. The difficulty of keeping the liquid in the sample space is solved by guiding the contact wires through the bottom anvil. 12 Cu insulated wires (25 μm in diameter) are fixed around the support cone by stycast epoxy, bonded to the sample and lead at one end and guided out of the pressure cell

through the bottom anvil (see Figs. 7 and 8). This arrangement is used for the electrical resistivity measurement by the standard 4-probe method. The reason why 12 wires are used instead of only 8 necessary (6 wires for each instead of 4 for each) is because of the high risk of losing contacts during the experiment (4 wires are essentially spares). We used Daphne Oil 7373 as the pressure exchange medium. Technical parameters of this cell allow us to reach pressures up to 6 GPa, using the load of several thousand kilograms. The sample space is, due to technical difficulties, limited in its height, leaving room for plate-like samples of ideally 100 μm or less in thickness. Body of the cell is made of MP35N (nickel-cobalt base alloy) and so is the outer gasket. The inner gasket, with an inner diameter of 2 mm, is made of CuBe.
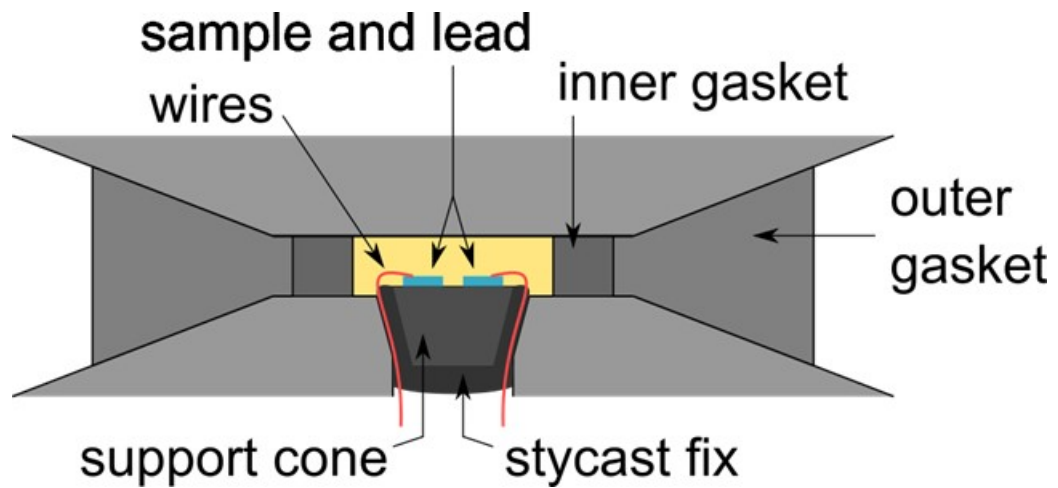

Fig.7: Scheme of the hydrostatic l-BAC with a sample, lead and contact wires (side view).
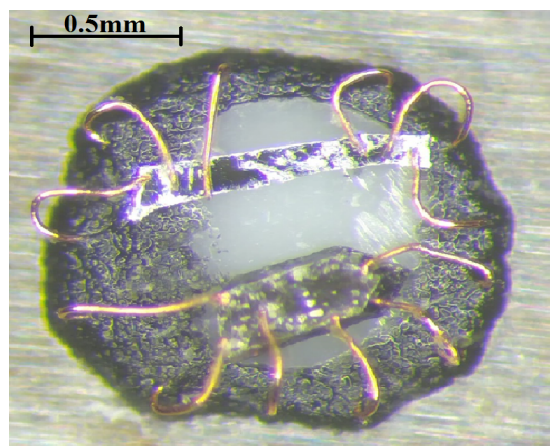

Fig.8: Experimental montage of the sample space in the hydrostatic l-BAC (top view). Cu wires are coming out of the stycast epoxy and are bonded to the thin lead resistor (top) and the CeRhSi$_3$ sample (bottom) which lay on the support cone.

Second type of BAC employs a solid pressure medium to transmit pressure within the sample space – s-BAC, in our case 2 discs made of steatite (see Fig.9). s-BAC creates the so called quasi-hydrostatic conditions throughout the experiment. Another difference compared to the l-BAC is that wires are guided through the gasket, not the anvil. Three s-BACs with different diameter of the gasket/sample space corresponding to different maximum pressure are standardly used (all with a same maximum load of about 1500 kg). Largest cell has a gasket diameter of 3 mm, sample space diameter of 2 mm and maximum pressure of 6 GPa. Medium size cell with diameters of 2 mm and 1mm, respectively, reaches the pressure up to 12 GPa and the smallest one with diameters of 1.5 mm and 0.7 mm can be utilized to apply pressure up to 20 GPa. The sample space shown in Fig.10 is demarcated on the bottom steatite disc by the gasket made of pyrophyllite. Sample and lead are fixed on the top of the steatite disc and arranged in ideally the same distance from the centre. This is important because of the quasi-hydrostatic conditions, which result in difference in pressure along the sample space radius (see Fig.2 and text in section 1.1. External Pressure). Wires made of Pt (non-insulated, 20 μm in diameter), which are flattened and sharpened at the end, are guided through the gasket. Unlike in the l-BAC, wires are not bonded, but merely placed on top of the sample/lead. The contact is made after the application of load. Guiding too many wires through the gasket worsens its stability and endangers the experiment, therefore it is preferable to connect the sample and lead, using only one pair of wires for the current. In this case, 4-probe method requires a minimum of 6 wires, but preferably 8 can be used, giving us 2 spares. Sample space height is strongly limited, allowing to accommodate the samples less than 50 μm thick.
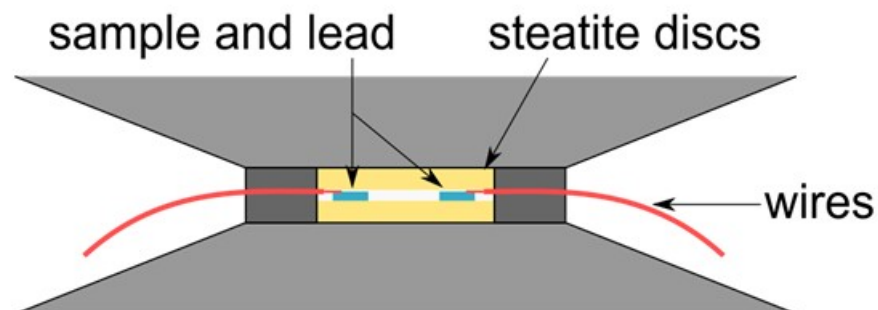
Fig.9: Scheme of the quasi-hydrostatic s-BAC with a sample, lead and contact wires (side view).
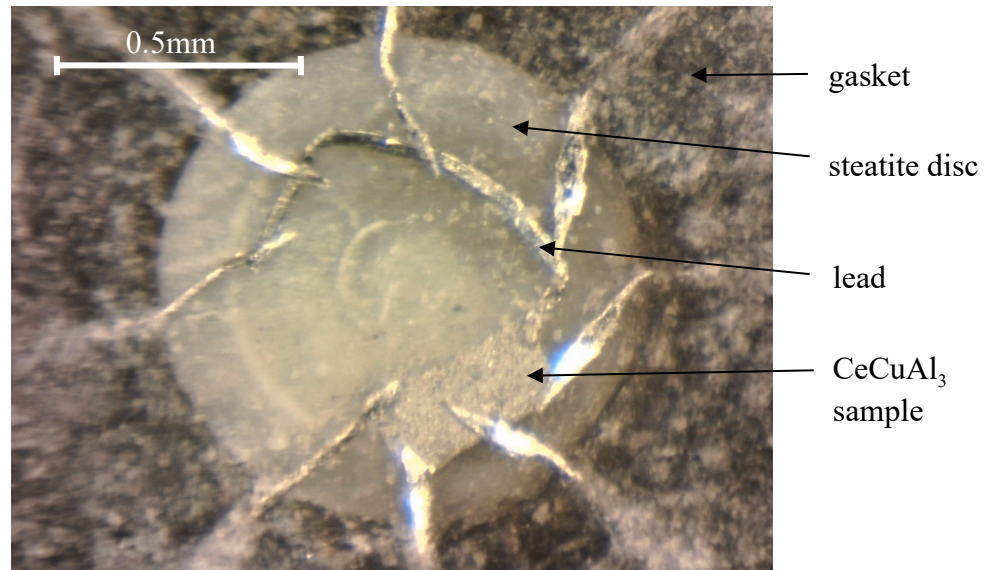
Fig.10: Experimental montage of the sample space in the quasi-hydrostatic s-BAC (top view). Medium sized s-BAC with a maximum pressure of 12 GPa.
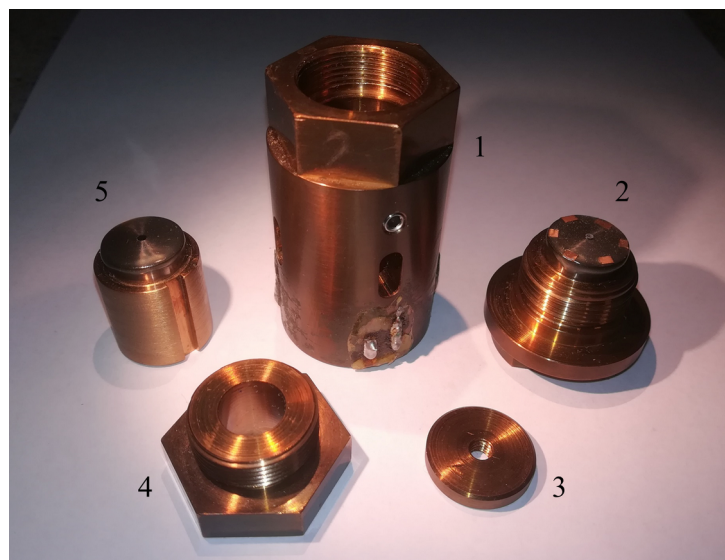
Fig.11: Components of the quasi-hydrostatic s-BAC: 1. body of the s-BAC, 2. bottom anvil with its support, 3. top support, 4. top support backup, 5. top anvil with its support.

2.3.2. Hybrid piston-cylinder cell

Mainly for the purpose of pressure media calibration, we used a piston-cylinder type hybrid CuBe/NiCrAl pressure cell which is commercially available (produced by C&T Factory Co., Ltd.) [15]. With an inner diameter of 4 mm, this cell can safely reach pressures up to 3 GPa. Sample space is situated in a Teflon cell, which has an inner diameter of 3 mm and keeps the liquid pressure medium from leaking out.

Wires are led through the plug which closes the Teflon cell. Pressure is then applied directly on the Teflon cell by the piston. Compression of the liquid medium results in an effectively usable length of the sample space about 9 mm. Compared to BACs, large volume of the sample space is undoubtedly a big advantage of piston pressure cells, though significantly reducing the maximal achievable pressure.
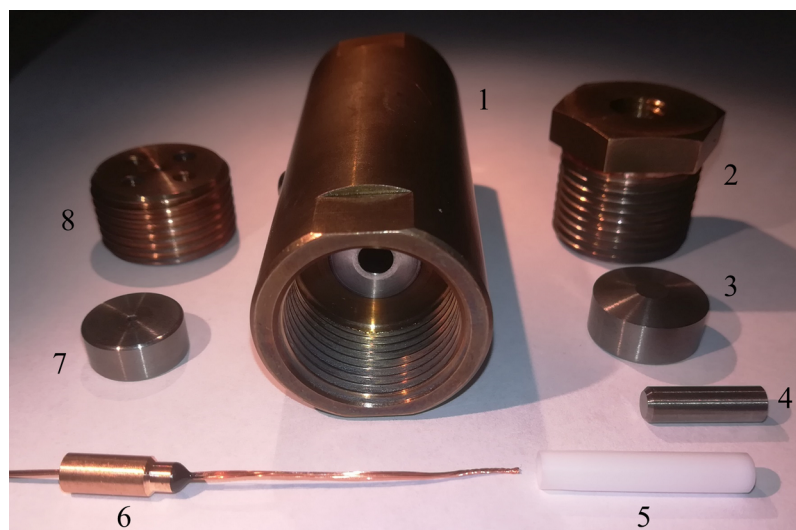
Fig.12: Components of the hybrid piston-cylinder pressure cell: 1. hybrid cylinder, 2. piston backup support, 3. piston backup, 4. piston, 5. Teflon cell, 6. plug (with Cu wires fixed in stycast epoxy), 7. plug backup, 8. plug backup support.

For a detailed calibration of the liquid pressure media (see section 2.3.3. High pressure media), multiple components were used simultaneously in a single experiment. The data measured employing various methods (see section 2.3.4. Pressure determination) therefore correspond to the same conditions inside the sample space. For the purpose of determining pressure at different places of the sample space and thus judging the quality of hydrostaticity, 3 manganin manometers were used. 1 lead manometer was employed for low temperature pressure determination. Lastly, 2 strain gauges were arranged along and perpendicular to the cell body axis in order to detect the solidification of the media. Together, 20 wires were used, determining resistance of each of 6 components (3 manganin manometers shared the current wires).

Fig.13: Experimental arrangement in the piston-cylinder cell, for the calibration of a liquid pressure medium. Lead resistor goes through the middle manganin coil. Strain gauges have their respective sensitive directions perpendicular to each other.
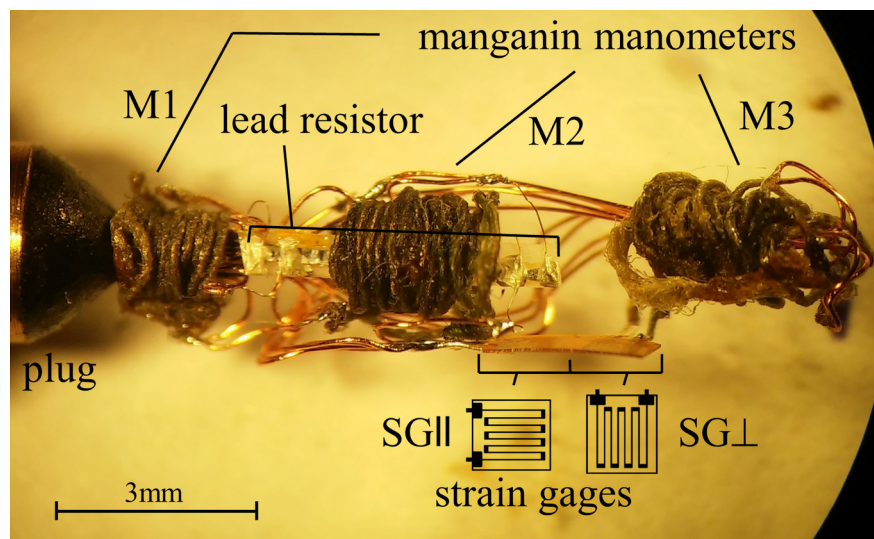
2.3.3. High pressure media

Pressure exchange medium (PEM) fills the sample space and surround the sample in an attempt to provide ideally hydrostatic conditions. They can be categorized as gas, liquid or solid PEM. Gas PEM provide the most hydrostatic conditions, but are accompanied by serious technical difficulties in their handling. Liquid and solid PEM are less difficult to use in experiments, but often produce non-hydrostatic behaviour in a form of sheer stresses (see section 1.1. External Pressure and Fig.1), as most liquids tend to solidify at higher pressures or/and low temperatures.

In this work, a solid PEM steatite is used in the quasi-hydrostatic s-BACs. Known as "the softest rock", steatite in form of a disc is squeezed between anvils while surrounded by a gasket. Difference in the hardness results in steatite filling the sample space to provide pressure redistribution.

Liquid pressure media used and studied in this work are 3 oils from the Daphne Oil 7000 series. These are specialized oils (produced by Idemitsu, Tokyo, Japan) solely for the high pressure experiments, possessing properties such as high solidification pressure, low compressibility, minimal volume change during solidification, chemical neutrality and are electrically insulating. Oldest and most commonly used Daphne Oil 7373 is known to solidify at room temperature under pressure of about 2.2 GPa [16]. Newer Daphne Oil 7474 was studied in detail at high temperature ($\geq$ 300 K) only, revealing a solidification pressure of about 3.7 GPa at

room temperature [17]. Lastly, the newest Daphne Oil 7575 was released to substitute Daphne Oil 7474. As of yet, the only information known about this oil is that it solidifies at pressures about 3.9-4.0 GPa at room temperature [18].

2.3.4. Pressure determination

Calculating pressure from (1) is not sufficient for the high pressure experiments. Pressure determination is normally done by calibrating pressure cells with known pressure dependent anomalies in various materials or by using in-situ pressure sensors (manometers).

Commonly used manometer for pressure determination during cell pressurizing at room temperature is a coil made of manganin wire (approximately 86% of Cu, 12% of Mn and 2% of Ni). It has a pressure dependent resistance and the actual pressure can be calculated from its change as

$$p = \frac{R(T,p) - R(T,0)}{R(T,0)} \frac{1}{\alpha(T)}. \tag{14}$$

Pressure coefficient $\alpha(T)$ slightly differs for each batch of produced manganins, but it should be stable for manganins within the same batch. Knowing the temperature dependence of $\alpha(T)$ and $R(T,0)$, it is possible to determine pressure in temperatures lower than ambient one [19], but with considerably higher uncertainty. Stabilized manganin manometers have a known experimental error of about 0.05 GPa when used at room temperature.

For the determination of pressure at low temperatures, SC transitions of pure elements are commonly used. Lead resistor was employed in our work for this purpose. Lead is SC at 7.19 K at ambient pressure [20] and, similarly to most conventional superconductors, its critical temperature decreases with increasing pressure. The width of the SC transition gives information about the hydrostaticity achieved in the experiment. PEM in liquid state usually shows a full transition well within a 0.03 K interval, whereas quasi-hydrostatic conditions tend to reveal a much broader transition in order of 0.1 K or larger. A pressure determination employing the SC transition of lead has a comparable uncertainty to the manganin manometer at room temperature.

Finally, there exist a few techniques capable to distinguish between solidified and liquid state of PEM by the hydrostaticity, e.g. $Ba(Fe_{1-x}Ru_x)_2As_2$ single crystals which have highly sensitive resistivity to non-hydrostatic environment [21]. To

investigate the hydrostaticity in detail, we employed miniature strain gauges (SG) which can be used to measure compressibility of materials [22]. SGs have one sensitive direction (see Fig.13) in which the strain is determined by their relative resistance:

$$r_m = G\varepsilon ,\qquad\qquad(15)$$

where G is a strain gauge factor. Therefore, the strain gauge is a viable tool for a detection of non-hydrostatic conditions tied with a solidification of PEM.

3. Previous results

Present study focuses on two Ce-based intermetallic compounds; $CeRhSi_3$ and $CeCuAl_3$, which are part of a large family of Ce-based intermetallic compounds with a 1-1-3 stoichiometry, $CeTX_3$, where T stands for a transition d-metal and X is a p-metal. The physical properties as valence fluctuations ($CeRuSi_3$ [1]), heavy-fermion (HF) antiferromagnetic (AFM) ordering, superconductivity ($CeCoSi3$ [1]), pressure induced superconductivity in lattices without inversion symmetry ($CeRhSi_3$ [2] and $CeIrSi_3$ [3]) or the so-called vibron quasi-bound state (postulated in $CeCuAl_3$ [4]) stay behind a continuous scientific interest in $CeTX_3$ intermetallics. In further text, we focus on previous results on $CeRhSi_3$ and $CeCuAl_3$, particularly with respect to their physical properties under pressure.

3.1. Crystal structure

Both $CeRhSi_3$ and $CeCuAl_3$, similarly as numerous other compounds from the $CeTX_3$ family, crystalize in ordered non-centrosymmetric tetragonal structure of $BaNiSn_3$-type, space group *I 4 m m*, No. 107 (see Fig.14 for illustration). The materials without the inversion centre were believed not to be consistent with a superconducting state (spin-triplet pairing requires a parity of unit cell). Indeed most HF superconductors crystallize in a centrosymmetric crystal structure [23]. However, several superconductors adopting a lattice without the inversion symmetry have been reported, e.g $CePt_3Si$ [5], $CeIrSi_3$ [3] or $CeRrSi_3$ [2]. The superconductivity in these materials cannot be explained by a standard singlet-triplet pairing, spin and orbital contributions cannot be treated independently [2,24]. It is believed that the spin-orbit-coupling plays a significant role in formation of superconductivity in these materials. Therefore, HF SC materials with a lack of inversion symmetry, e.g. crystallizing in the $BaNiSn_3$-type structure, became of considerable interest to the scientific community. The study of those compounds and search for the SC in other member of the family are the subject of present thesis.

Although $CeCuAl_3$ have been confirmed (at least in a majority of the single crystal) to crystallize in ordered $BaNiSn_3$-type structure [25], a structural instability may be present in this compound, considering mainly the parental structure of $BaAl_4$ type and its other derivates shown in Fig.14. The parent structure as well as $ThCr_2Si_2$ and $CaBe_2Ge_2$-type structures (all centrosymmetric) dictate the individual elements

in 113 compound to (partially) share the Wyckoff position with other elements. Previous reports on CeCuAl$_3$ proposed a ThCr$_2$Si$_2$ structure with 1/3 of Al atoms being randomly distributed over the 2a position [26]. Also the BaAl$_4$ structure was determined as a structure of CeCuAl$_3$ in earlier study [27]. All these structure types (could) have the same lattice parameters, which, together with a low sensitivity of powder X-ray diffraction to Cu/Al occupation, prevent a precise determination of the CeCuAl$_3$ structure. On the other hand, neutron diffraction experiment, being more sensitive to Cu/Al positions, preferred BaNiSN$_3$ structure [25].

Recent NMR study on a La analogue, LaCuAl$_3$, revealed multiple different La environments in the spectrum of this compound [28]. The BaNiSn$_3$ phase formed the majority of the sample, however also other variants were clearly manifested. In contrast the single La environment (BaNiSn$_3$-type) was observed in LaAuAl$_3$ [28]. Of course, the presence of additional structural variants would significantly affect the physical properties of the compound. Pressure induced SC in materials without inversion symmetry is a phenomenon highly sensitive to actual structure. Hence, any structural instability in CeCuAl$_3$ may explain why no SC was yet measured in this compound, despite its similarities to pressure induced superconductors CeRhSi$_3$ [2] or CeIrSi$_3$ [3]. Nonetheless, the other explanation, which motivated us to perform present study, is found in insufficient experimental conditions, low temperature and high pressure [29,30,31].

Crystal structure of CeRhSi$_3$ was determined to be of the BaNiSn$_3$-type [2,24,32]. No other structure has been reported. The structure stability of CeRhSi$_3$ (and LaAuAl$_3$) could be tentatively ascribed to a significant mass difference between Rh and Si (Au and Al), contrary to Cu and Al in CeCuAl$_3$.
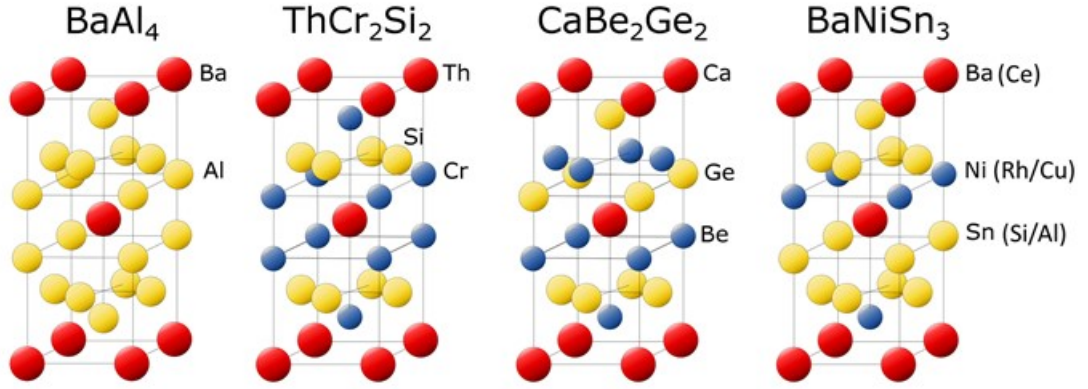
Fig.14: Parent tetragonal BaAl₄–type structure (with an inversion symmetry) and its 3 subgroups, $ThCr_2Si$ and $CaBe_2Ge_2$ also with a centre of inversion, and $BaNiSn_3$-type without the inversion symmetry.

3.2. $CeRhSi_3$

$CeRhSi_3$ orders antiferromagnetically bellow 1.6 K at ambient pressure. Upon the application of pressure, $CeRhSi_3$ becomes SC with a maximum of the observed T_c of about 1.1 K. A number of studies on the pressure induced SC, magnetic and transport properties, as well as CEF was performed on $CeRhSi_3$ [2,24,32]. Ambient pressure studies showed a Néel temperature independent on magnetic field along the c axis and a slight decrease of T_N was followed for external magnetic field applied along the a axis (see Fig.15).
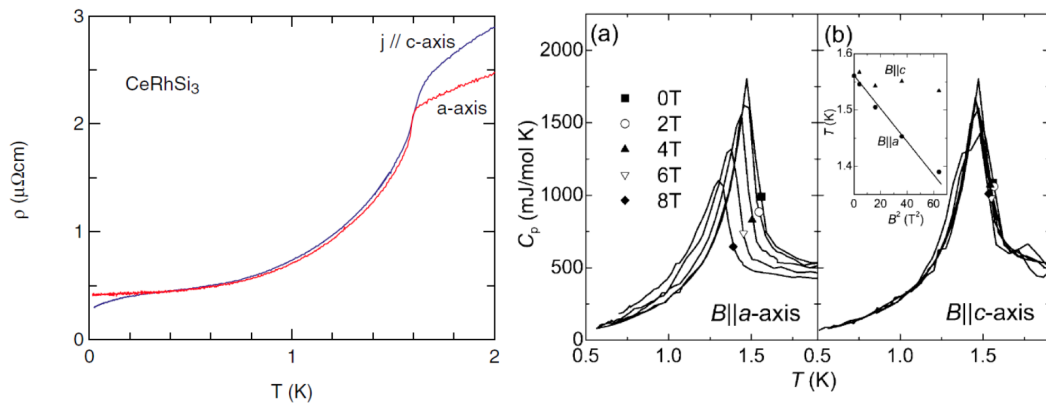

Fig.15: Ambient pressure properties of $CeRhSi_3$. On the left, temperature dependence of electrical resistivity with a kink at $T_N = 1.6$ K, typical for magnetic ordering of the compound [24]. On the right, heat capacity measurements in different magnetic fields applied along the (a) a axis and (b) c axis [32].

The anisotropic behaviour is demonstrated also in electrical resistivity data: Pressure induced SC emerges around 1 GPa for j (electrical current) applied along the a axis [24], while along the c axis it can be observed in much lower pressures, with first signs being visible even at ambient pressure (see Fig. 16). T_N increases with pressure at first (up to 1 GPa), and quickly starts to decrease at higher pressures [2,24]. The anomaly corresponding to the AFM transition ultimately disappears as it merges with SC transition above 2 GPa and is no longer observable. The emergence of SC transition is quite continuous, as the shape of the transition reaches the standard SC sharpness when T_c merges with T_N, being at its maximum. Investigating carefully the data measured with j along the a axis allowed to follow the pressure evolution of additional anomaly at temperature T^*. The anomaly was observed also on temperature evolution of ac-susceptibility measured with magnetic field applied along the a axis. Both types of measurement along the c axis revealed a single SC transition. The presence of the additional anomaly was discussed in [2,24] assuming both intrinsic temperature development of the SC transition and sample quality. All high pressure experiments on $CeRhSi_3$ were done up to 3 GPa in hybrid-cylinder piston pressure cell. According to previous results [2,24], T_c reaches the maximum around 2.6 GPa and is expected to decrease at higher pressures above 3 GPa (see Fig.17). The measurement at pressures higher than 3 GPa was, nevertheless, missing, and is the subject of our present study.
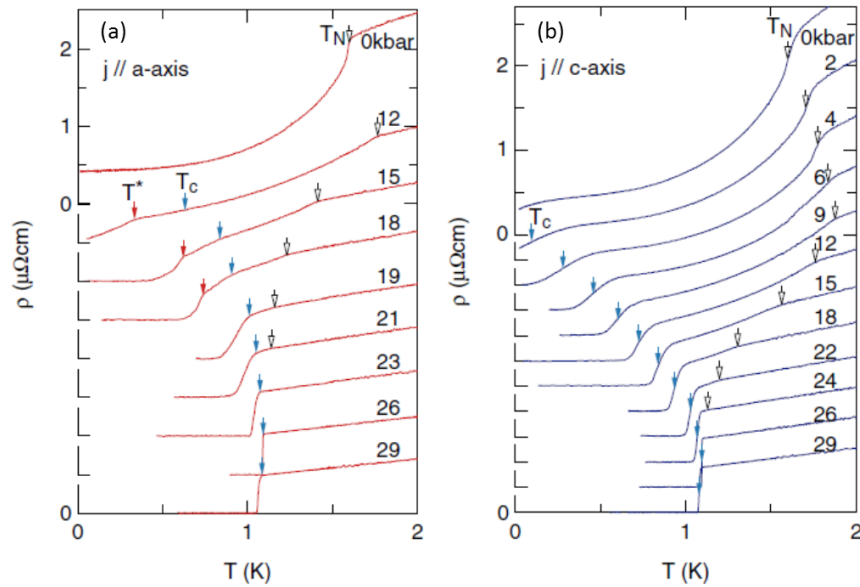

Fig.16: The emergence of pressure induced SC in $CeRhSi_3$ single crystal with j applied along the (a) a axis and (b) c axis [24].
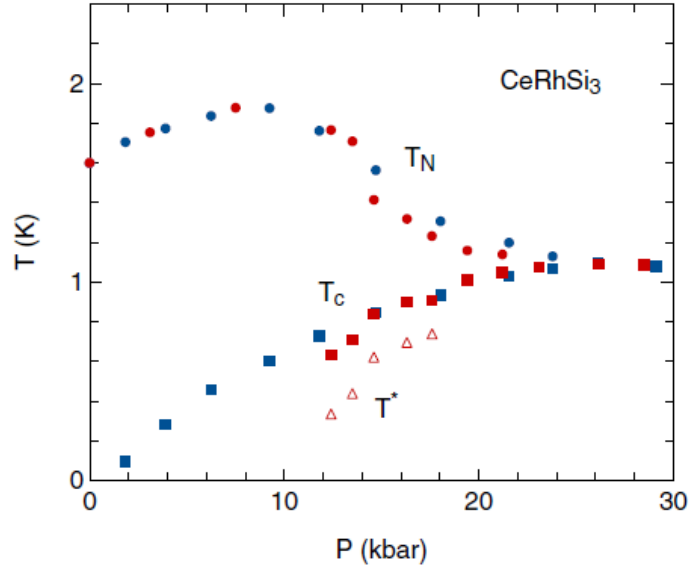
Fig.17: Phase diagram of CeRhSi$_3$ featuring SC critical temperature, Néel temperature and anomalous T* at pressures up to 3 GPa. Red symbols stand for data measured with j applied along the a axis and blue symbols for data along the c axis [24].

The influence of magnetic field on superconducting transition was measured under constant pressure of 1.5 GPa and 2.6 GPa [2,24], where a maximum value of T$_c$ was observed. At 1.5 GPa, both T$_c$ and T* shift to lower temperatures with increasing field and disappear before magnetic field reaches 7 T, while T$_N$ shifts to slightly higher temperature in applied magnetic field. At 2.6 GPa, SC transition is sharp and clearly pronounced up to almost 8 T (see Fig.18).

Fig.18: (a) Resistivity as a function of temperature for different static magnetic fields, applied along the a axis. (b) *T-H* phase diagram illustrating the shift of SC transition with applied field [24].

3.3. CeCuAl₃

CeCuAl$_3$, with a Néel temperature of $T_N \sim 2.7$ K (sample dependent, more notable difference between single crystals and polycrystals [33]), was identified as a HF antiferromag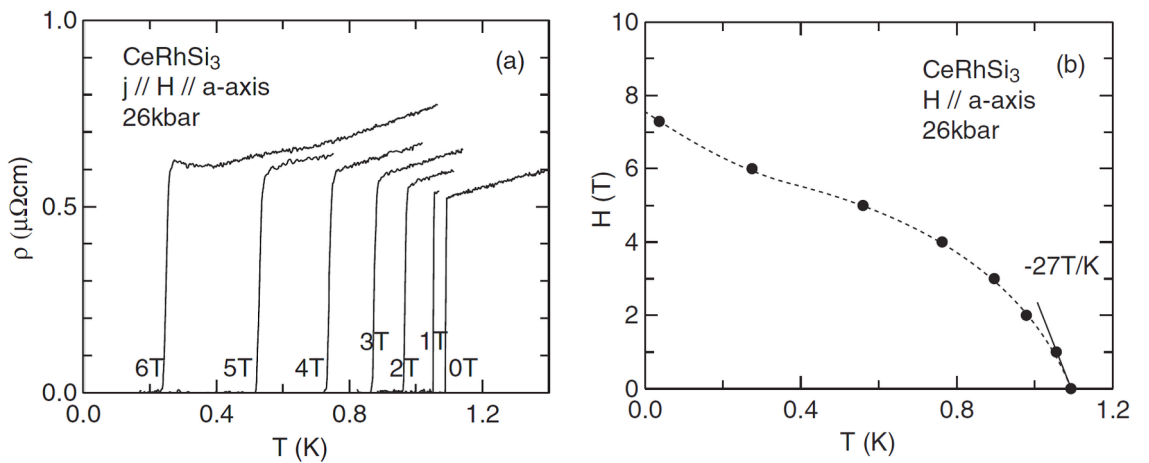net [34]. However, considering the low-energy CEF excitation at 1.5 meV [4,35], CeCuAl$_3$ can be considered as a standard metal. CEF energy scheme, further, revealed additional magnetic excitations in course of the inelastic neutron scattering (INS) experiment. Contrary to expected CEF spectrum for Ce-based compound (see section 1.4. Crystal electric field), three CEF excitations were observed [4,35] (see Fig.19). The so-called vibron quasi-bound state model, first introduced by Thameier and Fulde to explain additional CEF excitation in the cubic CeAl$_2$ [36], was generalized for the tetragonal structure of CeCuAl$_3$ to explain its energy spectrum [4]. The model supposes a strong coupling between lattice and orbital degrees of freedom leading to a new quantum state – vibron. A fragile balance of the system can be disturbed by e.g. a substitution of Cu-Al leading to a standard CEF scheme [35] (see Fig. 19).
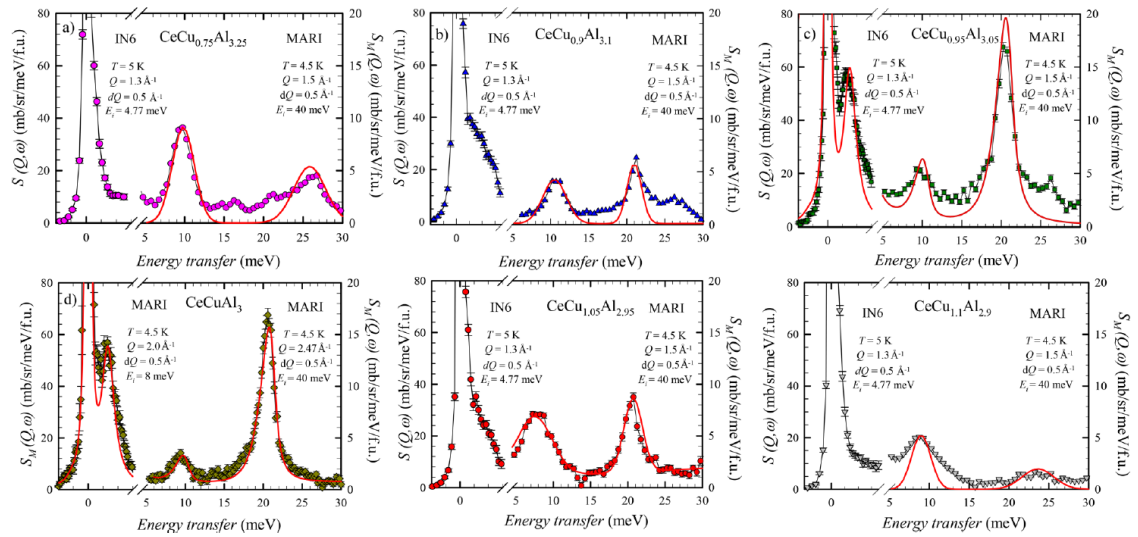
Fig.19: Effect of chemical substitution on CEF peaks observed by INS. In panels c) and d) three-peaks spectra were observed. A standard CEF splitting derived from the tetragonal structure is seen for compositions in panels a) and f). Panels b) and e) depict the spectra on the border between the two CEF schemes [35].

Similar properties – crystal structure, metallic behaviour, AFM ordering – of CeCuAl$_3$ and pressure induced SCs CeRhSi$_3$ [2] and CeIrSi$_3$ [3] raised suspicion about a possible pressure induced SC also in CeCuAl$_3$. Such suspicion is invigorated

also e.g. by our recent study on the compressibility of CeCuAl$_3$ [22]. The crystallographic lattice is more compressible along the *c* axis than along the *a* axis, implying that the application of high (hydrostatic) pressure will result in the c/a ratio closer to that of CeRhSi$_3$ or CeIrSi$_3$.

High pressure experiments focused on magnetic and transport properties, and anticipated SC transition, were carried out on polycrystalline CeCuAl$_3$ [29,30,31]. The experimental conditions were severely limited: pressures up to 3 GPa at temperatures down to ~ 1 K or pressures up to 8 GPa at temperatures down to 2 K [31]. The magnetic and transport measurements revealed the T$_N$ increasing with increasing pressure. Opposite development was followed on NMR data [37] (see Fig.21). Other than anomaly corresponding to T$_N$, a broad maximum was observed in ρ(T) above 10 K together with a faint anomaly at higher temperatures (140 K). Those anomalies were attributed to Kondo effect influenced by CEF [30]. The external pressure then enhances the Kondo effect, resulting in pressure development of the anomalies.

Pressure dependence of all three anomalies becomes most intriguing at pressures between 6 and 8 GPa. The anomaly corresponding to AFM ordering is no longer visible under 8 GPa. Concurrently, the other two anomalies seem to merge into one broad maximum (see Fig.20). No sign of superconducting transition was observed in those studies [29,30,31].
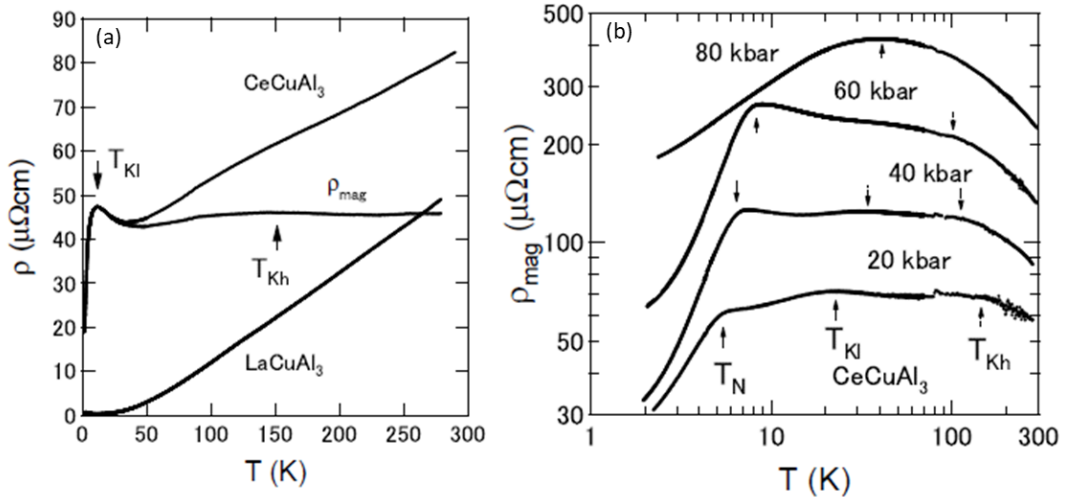

Fig.20: (a) Temperature dependence of electrical resistivity of CeCuAl$_3$ and its non-magnetic analogue LaCuAl$_3$ at ambient pressure. (b) Development of magnetic contribution to electrical resistivity at high pressures [31].
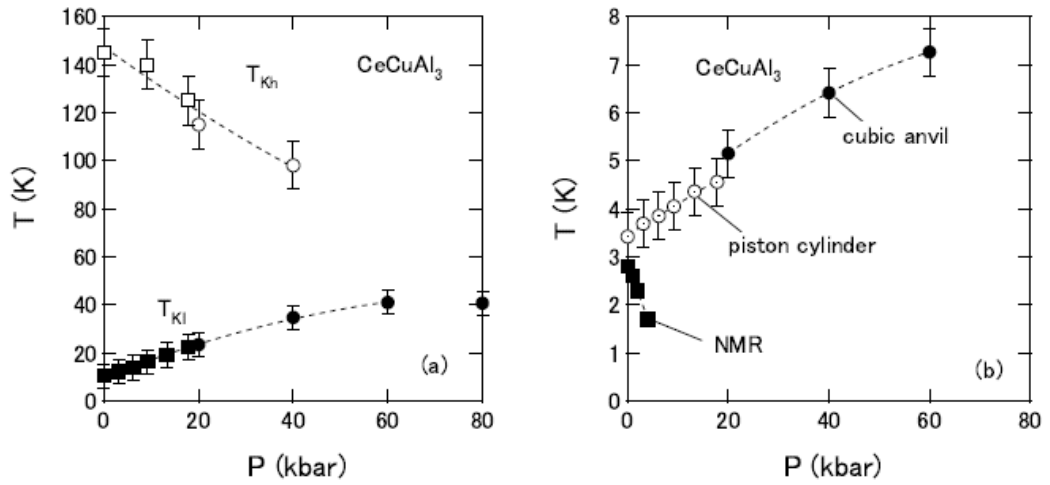
Fig.21: (a) Pressure development of T_{Kh} and T_{Kl} and (b) T_N as determined from electrical resistivity measurements on polycrystalline sample [31].

4. Results

4.1. CeRhSi$_3$

4.1.1. Sample preparation and characterization

CeRhSi$_3$ single crystals were grown by the flux growth method, more specifically a true-Sn-flux was used as the solvent. All single crystals had a tendency to grow in the form of relatively thin plates along one particular direction, forming clear facets (see Fig.22a). Top-right crystal in Fig.22a grew along two perpendicular directions. Such a growth can be easily explained assuming that the growth directions are perpendicular to the c axis, i.e. 4-fold rotation symmetry. EDX analysis documented the correct composition and homogeneity of the samples. Remnants of Sn flux on the surface of single crystals (Fig.22b) were manually disposed of by polishing.
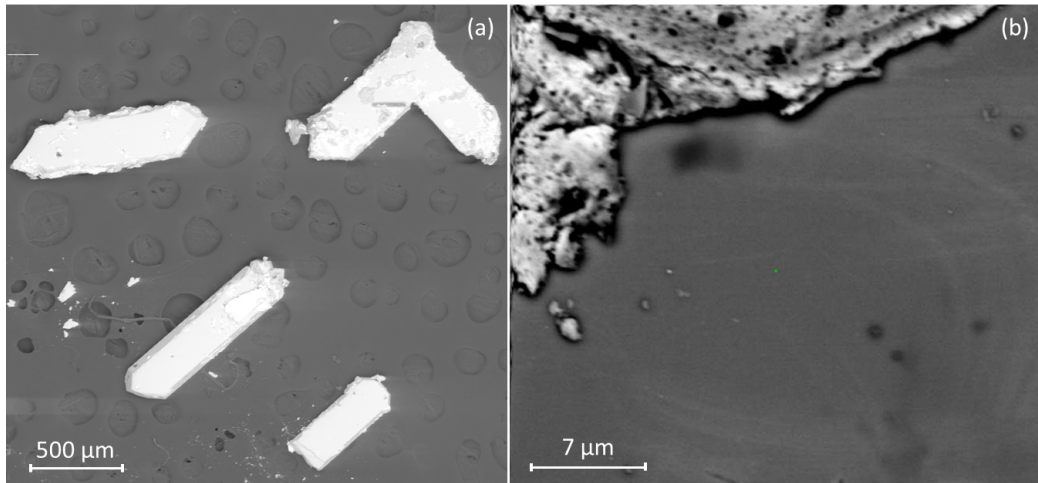
Fig.22: As-cast CeRhSi$_3$ single crystals viewed with SEM. (a) low magnification, growth tendency along one direction is observed. (b) large magnification, homogenous surface with remnants of Sn flux on the top-left part of the image.

Laue X-ray diffraction confirmed the prepared samples being single crystals, and allowed to reveal their orientation. All the sample grew in the same orientation (three different samples were investigated by Laue diffraction and further used for the transport measurements). The c axis was unambiguously identified, observing 4-fold symmetry on Laue image (Fig.23), to be perpendicular to the surface shown in Fig.22, i.e. the thinnest dimension of the sample (about 0.1 mm for all samples).

Somewhat surprisingly, the preferential growth direction (and simultaneously the direction perpendicular to it and to [001]) was determined not to be the [100] direction (the *a* axis), but the [110] crystallographic direction. As the dimensions of usable samples were very limited, the only reasonable option for electrical resistivity measurements (section 2.3.1. Bridgman anvil cells) was a 4-probe montage with electrical current applied along the growth direction (in some cases up to 1 mm long). As such, all resistivity data were measured along the [110] axis, which should bear more resemblance to data measured previously along the *a* axis rather than those with current parallel to the *c* axis.
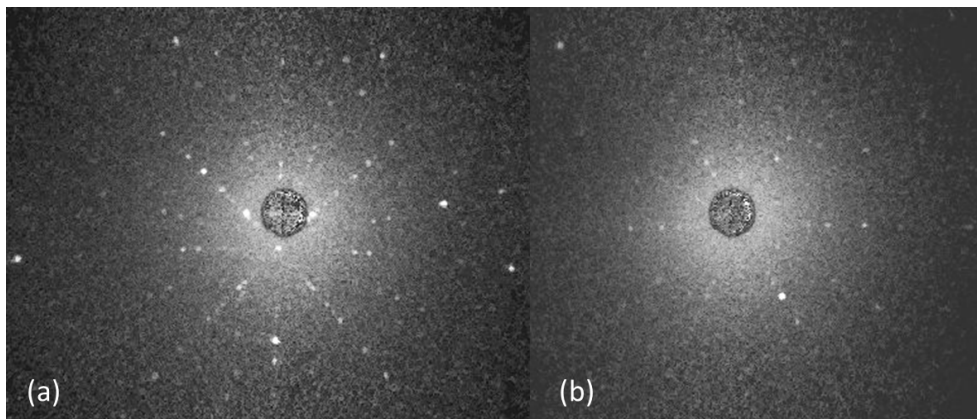
Fig.23: Laue diffraction images of $CeRhSi_3$ single crystal (a) along the *c* axis (4-fold symmetry) and (b) along the [110] direction (2-fold symmetry). The images quality is relatively low due to small dimensions of the single crystal and used diffractometer.

Heat capacity and transport properties at ambient pressure were measured as another part of the characterization routine, because the measured data can be easily compared to the previously published data on $CeRhSi_3$. The heat capacity was measured down to 0.4 K employing Physical Property Measurement System (PPMS, Quantum design) [12] and a standard time-relaxation method on sample of 0.14 mg mass. The contributions of used specific heat puck and apiezon N grease, used to attach the sample to the puck, were subtracted from measured data to obtain pure sample specific heat. PPMS and 4-probe method were used for electrical resistivity measurement, also down to 0.4 K. The magnetic field was applied along the [001] crystallographic direction in both cases.

Temperature development of heat capacity revealed a pronounced lambda anomaly at T_N = 1.6 K, representing the transition from paramagnetic to antiferromagnetic state (see Fig.24). Both the temperature development of the signal and its magnitude are well in agreement with previous results [32]. The "amplitude" of the anomaly is slightly larger in our case, which could be ascribed to better quality of the single crystal. Magnetic field up to 12 T applied along the *c* axis has a negligible impact on the specific heat anomaly; it shifts the anomaly slightly first to lower temperature – up to 2 T, and subsequently to higher temperature for higher field (inset of Fig.24). The observed behaviour is in agreement with T_N being effectively independent of magnetic field applied along the *c* axis as reported in [32].

A pronounced kink in electrical resistivity data confirmed the AFM phase transition at T_N (Fig.25). Although the electrical current was applied along the [110] direction, compared to previous experimental setting with *j* along the *a* or *c* axis [24], the development of measured electrical resistivity - including its magnitude and so called RRR factor, RRR = $R_{300K}/R_{0.4K}$ = 88 - is in good agreement with previous results.
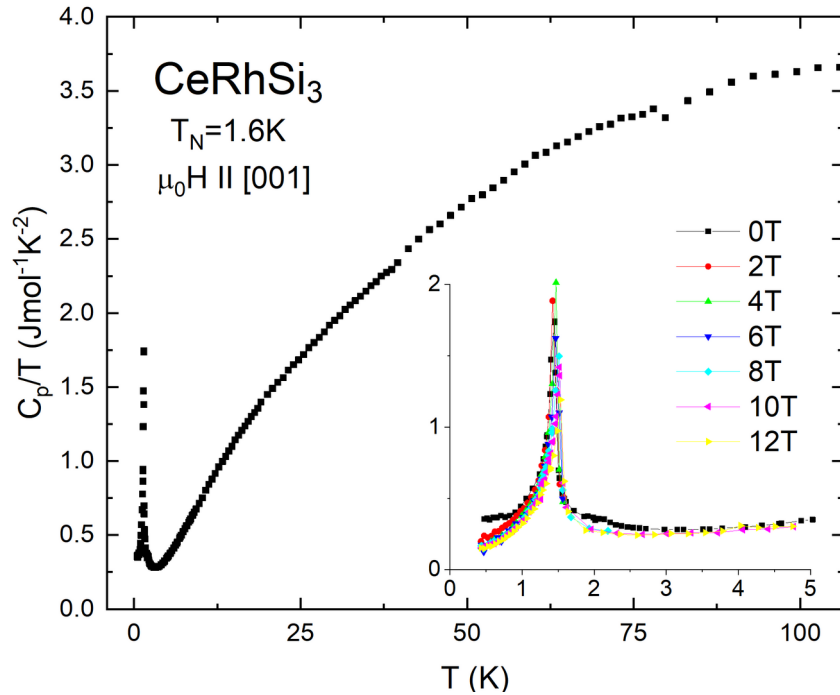
Fig.24: Specific heat of a CeRhSi$_3$ single crystal at ambient pressure. Inset shows zoomed low-temperature part of C$_p$/T(T) data, together with data measured in external magnetic field.
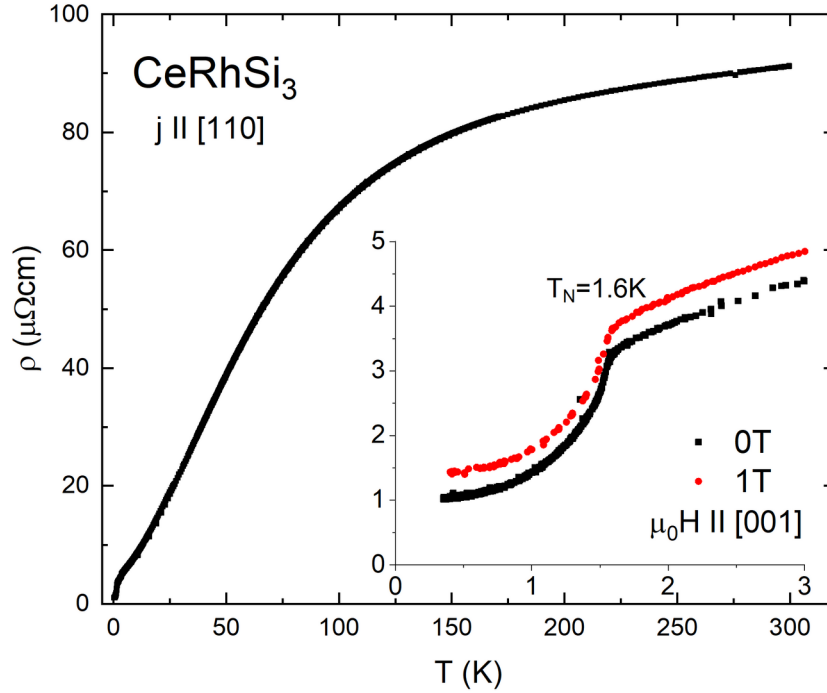
Fig.25: Electrical resistivity measured along the [110] direction on a CeRhSi$_3$ single crystal at ambient pressure. Inset shows $\rho(T)$ in magnetic fields applied along the [001].

Previous results were obtained on CeRhSi$_3$ single crystals grown by Czochralski pulling method [2,32,24]. At first, we attempted to prepare the single crystal employing the Czochralski method as well. However, both attempts were unsuccessful, as the powder diffraction patterns measured on grinded parts of the prepared ingots did not match the expected crystal structure. Instead, the patterns contained the signal of at least two phases, none of them being properly described by BaNiSn$_3$ model. On the other hand, EDX maps of sample surface showed relatively homogeneous distribution of elements. Aware of the sample bad quality, we performed both transport and magnetization measurements at ambient pressure. The measured data differed significantly from expected behaviour for CeRhSi$_3$, and moreover documented the samples consist of several phases. In contrast, the flux method allowed us to prepare good quality samples, as confirmed by above listed measurements. The small dimensions of single crystals are sufficient, and in fact preferable - the sample orientation is well defined, for experiments under external pressure.

4.1.2. Pressure induced superconductivity in $CeRhSi_3$

Pressure induced superconductivity in $CeRhSi_3$ was investigated by transport properties measurements, particularly pressure induced SC in yet unexplored pressure region above 3 GPa. Pressure cell of l-BAC type was used for the study, since it can potentially reach pressures up to 6 GPa while providing more hydrostatic conditions than s-BAC. Single crystalline sample was polished to a thickness of about 80μm and prepared for resistivity measurement under pressure (see Fig.8). The measurement was performed at temperature down to 0.3 K and in magnetic field up to 18 T in '20 T & 30mK' cryomagnet [12]. Pressure was determined by a lead manometer combined with a load calibration. We note, that three out of six leading wires on lead were lost during the measurement, i.e. the last two pressure points were discerned only by load calibration. Moreover, the usage of load calibration allowed to overcome uncertainties related to possible residual magnetic field in the cryostat, which would shift the SC transition of lead to lower temperatures and hence indicate higher pressure.

Behaviour of electrical resistivity of $CeRhSi_3$ at moderately low temperatures is similar under ambient pressure and higher pressures (see Fig.26a): Starting at room temperature, a decrease of resistivity is relatively small (subtle), and becomes notably steeper below ~150 K. Applying larger pressure results in more steep decrease of overall resistivity, reaching smaller values of resistivity at temperatures below ~150 K, while the resistivity in high temperature region gradually increases. Such development can be well understood considering the changes of crystallographic lattice under pressure. The applied pressure influences both interatomic distances and local environment of Ce ions, leading to changes of phonon as well as magnetic (crystal field) contribution to electrical resistivity.
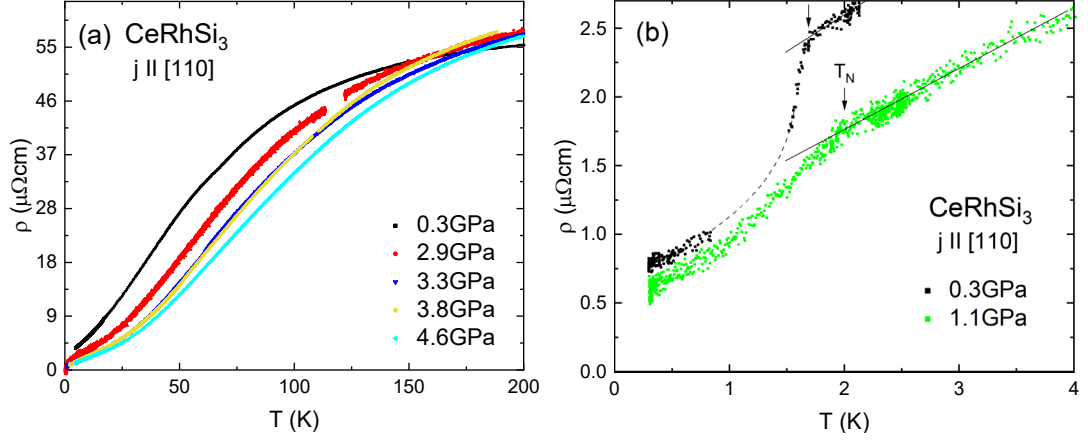
Fig.26: Temperature dependence of electric resistivity of CeRhSi$_3$ at several pressures (a) below 200K and (b) below 4K, illustrating the shift of Néel temperature T_N under pressure.

Focusing on the low-temperature interval of measured data (Fig.26b), a bump corresponding to AFM phase transition was observed at pressure 0.3 GPa, mostly resembling the resistivity development at ambient pressure (Fig.25). Increasing the pressure to 1.1 GPa, the transition became less pronounced and shifted to higher temperature. No AFM transition was detected at higher pressures; all in agreement with previous results [2,24]. Under 1.1 GPa there is no SC transition observed, however an unusual decrease in resistivity can be followed when nearing the lowest measured temperatures, which may indicate a start of a broad SC transition below 0.3 K. Such assumption is, in fact, well in agreement with previous results [2,24] as the SC transition is first observed at around 1.1 GPa.

The pressure induced SC is clearly observable under 2.9 GPa and higher pressures, see Fig.27. Similarly to previous results [2,24], a maximal value of T_c (about 1.1 K) is observed under this pressure. The change of electrical resistivity of the sample during the SC transition is sharp, on temperature interval of ~0.15 K. Further pressure application results in a continuous suppression of T_c, shifting it to lower temperatures, while the SC transition has a tendency to broaden (~0.45 K under 4.2 GPa). Under 4.6 GPa, the SC transition is suppressed to such lengths that it is not finished at 0.3 K.

Previously reported anomalous behaviour of SC transition (marked by temperature T*) observed in electrical resistivity measurements for $j \parallel a$ axis [2,24] was not exhibited in our data. There was no indication of additional/subsequent

transition at 2.9 GPa, in agreement with previous study [2,24]. The SC transition at higher pressures was broad, but smooth. Although we did not measure in pressure region from 1.2 to 2.0 GPa, and therefore cannot rule out the presence of T* anomaly at those pressures also in our sample (see Figs. 17 and 28), we tend to explain the additional anomaly to be sample dependent. Previously, the measurement was done on Czochralski grown single crystal, while the present study was performed on the high-quality flux-grown sample.

Technical difficulties resulted in a notable hysteresis between heating and cooling scans. Therefore, data in Fig.27 were gained from both heating/cooling curves utilizing the PF (percentile filter) smoothing.
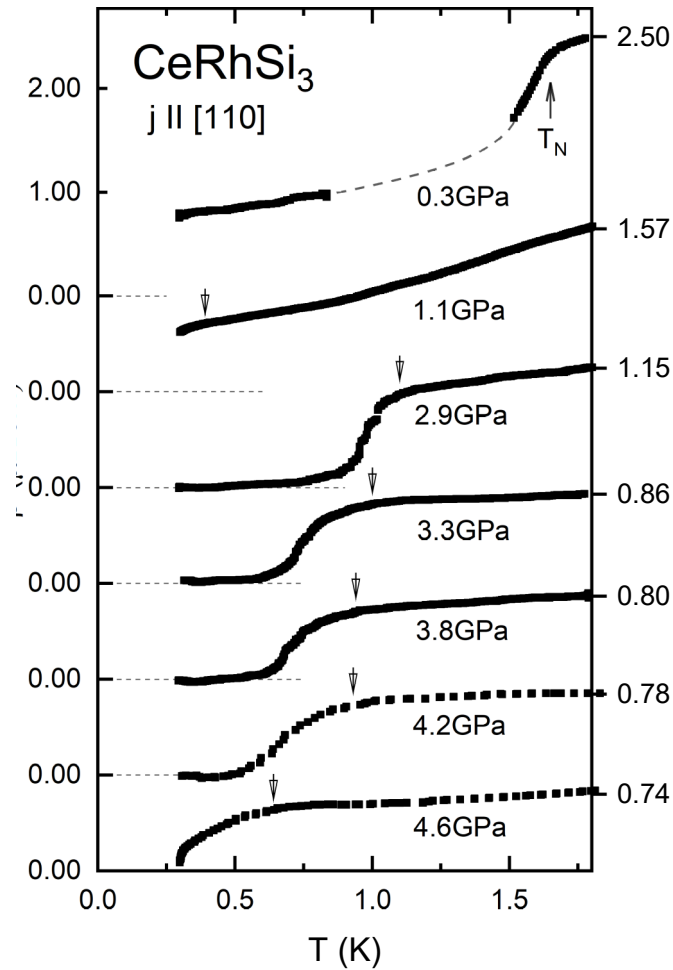

Fig.27: Electrical resistivity data with pronounced magnetic and superconducting transitions at several pressures. The arrows indicate the T_c used for construction of Fig.28.

Evolution of the pressure induced SC is illustrated in the *T-p* phase diagram, see Fig.28. We emphasize a difficulty to rigorously determine temperature T_c for

individual pressure points. This is due to a broad nature of the SC transition in high pressures. For the purpose of following the previous results [24], T_c was determined in the same way, i.e. at top of the SC transition. Just as the previous speculations about the pressure induced SC in this material predicted, gathered data show a characteristic dome behaviour, i.e. after reaching the maximum at 2.9 GPa, T_c gradually decreases under increasing pressure. Unfortunately the experiment came to the end (lower anvil broke apart) before we could confirm the complete disappearance of SC, at least at temperature as low as 0.3 K. Nonetheless, following the behaviour of electrical resistivity under 4.6 GPa and inspecting the phase diagram in Fig.28, we are convinced that SC in CeRhSi$_3$ will disappear in the pressure region between 5 and 6 GPa. Pressure development of T_N is in good agreement with previous data, considering the samples prepared by different methods and mainly the different direction of applied electrical current.
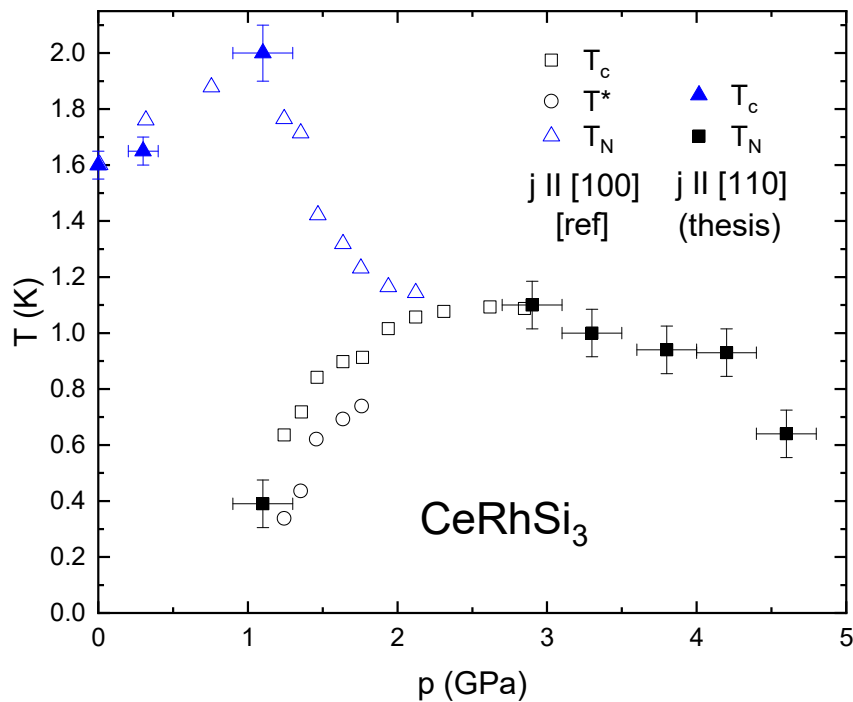
Fig.28: *T-p* phase diagram of pressure induced SC in CeRhSi$_3$, including data adopted from [24] (empty symbols).

At each pressure point, a suppression of SC transition by external magnetic field was investigated. Firstly, temperature scans of electrical resistivity in various magnetic fields were measured, see an example for pressure 2.9 GPa in Fig.29. In this particular case, pressure induced SC is strongly resistant to magnetic field

compared to higher pressures (see Fig.31). Starting with a sharp transition in zero field, continuous broadening of SC transition is observed with increasing magnetic field. Compared to the previous results (Fig.18), measured in magnetic field along the *a* axis, pressure induced SC survives up to notably higher magnetic field applied along the *c* axis. Moreover, based on the difference in sharpness of SC transition (and the broadening tendency) between 2.6 GPa [24] and 2.9 GPa (thesis), it seems that SC is already starting to be suppressed at 2.9 GPa. Therefore we believe that an even higher critical magnetic field may be present at 2.6 GPa along the *c* axis.
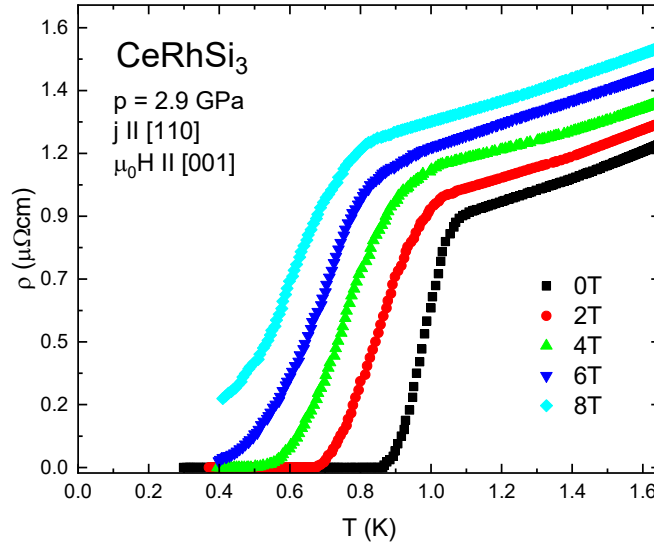
Fig.29: Temperature dependence of resistivity under external pressure of 2.9 GPa in several magnetic fields applied along the *c* axis. Smoothed data (Savitzky-Golay) plots.

The measurements in constant magnetic fields were complemented by magnetoresistance measurements. At each pressure point, the temperature was kept at lowest reachable value for the experimental apparatus, i.e. 0.28 K in zero field and 0.44 K in a field of 18 T. Magnetoresistance curves for each pressure point are presented in Fig.30. The SC transition shifts to lower temperature applying external pressure higher than 2.9 GPa. Surprisingly, there is a significant difference between SC transition under 2.9 GPa and all higher pressures; not only in magnitude of critical field, but also in the overall shape. Although the SC transition at 2.9 GPa is particularly large, the critical field μ_0H_c is unambiguously identified as a kink in 13 T. Observed behaviour is mostly consistent with previous results [24]. The measurement at 1.5 GPa showed a change of the transition from a broad one to

sharper one strongly depending on temperature. Moreover, an additional anomaly on the transition was introduced (H*). No such anomaly was followed in our data.
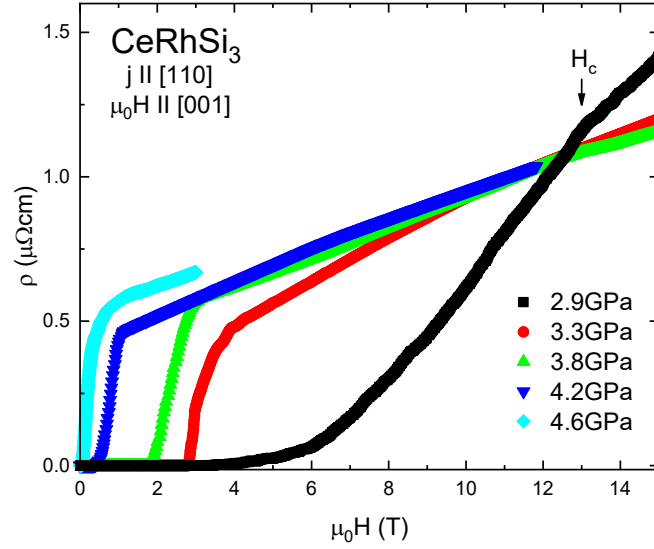
Fig.30: Magnetoresistance measurements at lowest achievable temperature (0.28 K in zero field to 0.44 K in strong fields). Smoothed data (PF) plots.

To sum up the results from measurements of the temperature and magnetic dependencies of electrical resistivity, a *H-T* phase diagram was constructed (Fig.31). Critical temperature/field was determined as the top of SC transition (deviation from local linear behaviour). Comparing our results at 2.9 GPa with the previous results at 2.6 GPa [24], SC persists up to higher magnetic field for field applied along the *c* axis than along the *a* axis, while the shape of SC phase border is similar in both cases. Moving to higher pressures, critical field is severely supressed unlike the moderately suppressed critical temperature. Possibly, the plateau of maximum critical temperature (~2.5-3 GPa, see Fig.28) is accompanied by unusually high perseverance against magnetic field. At pressures below 2 GPa, SC transition was reported to have unusual behaviour (e.g. under 1.5 GPa in Fig.31, [2]), which is described by two observed anomalies T_c and T*. This was supported by a similar result from ac-susceptibility measurements [2]. Although no additional anomaly was observed in our high pressure data (4.2 and 4.6 GPa), the values of critical field are comparable.
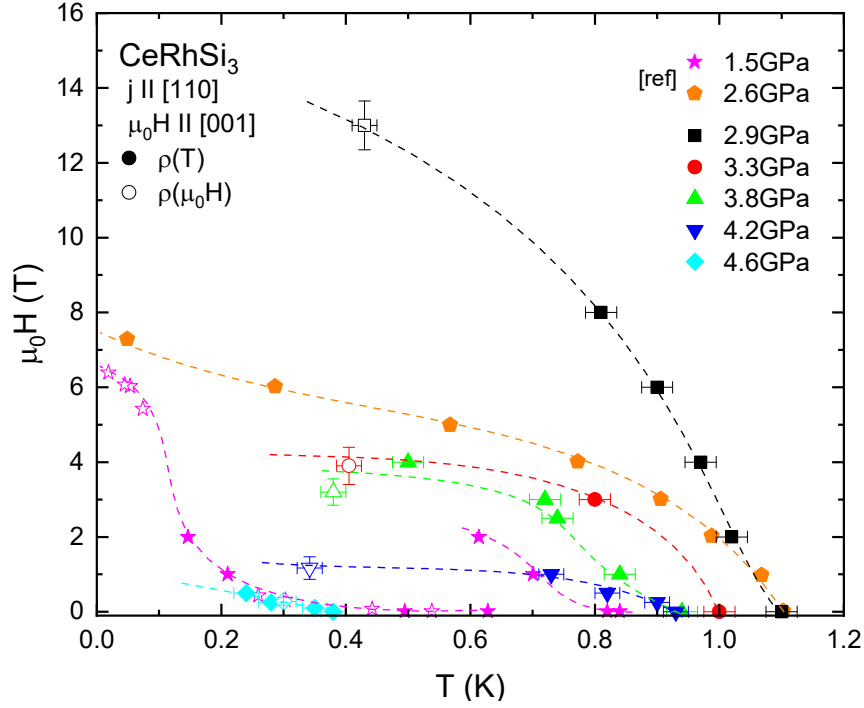
Fig.31: *H-T* phase diagram constructed from temperature (full symbol) and field (open symbols) dependencies of electrical resistivity of CeRhSi$_3$ at various pressures. Previous results (pressures 1.5 GPa [2] and 2.6 GPa [24]) were measured in magnetic field applied along [100] direction.

4.2. CeCuAl$_3$

4.2.1. Characterization

CeCuAl$_3$ single crystals of high quality were successfully grown at DCMP, utilizing the Czochralski method of crystal growth. Detailed characterization of these samples at ambient pressure was performed prior our present study [25,33,35]. The temperature and magnetic field dependencies of magnetization, specific heat and electrical resistivity were well in agreement with previous reports on CeCuAl$_3$ [29,30,31]. Moreover, the single crystal used for our high-pressure study was checked by Laue neutron diffraction experiment at Institute Laue-Langevin, Grenoble, documenting a good quality of the single grain crystal [33].

The prepared single crystal was oriented by Laue X-ray diffraction, cut and polished. The small samples were checked by Laue diffraction once again to confirm their proper orientation (see Fig.32). Moreover, their phase purity and homogeneity were once again verified by electron microscopy and EDX technique.

Fig.32: Laue diffraction images of CeCuAl$_3$ single crystal (a) along the *c* axis (4-fold symmetry) and (b) along the *a* axis (2-fold symmetry). The Lauegrams were collected on sample subsequently measured in s-BAC.

4.2.2. High pressure results on CeCuAl$_3$

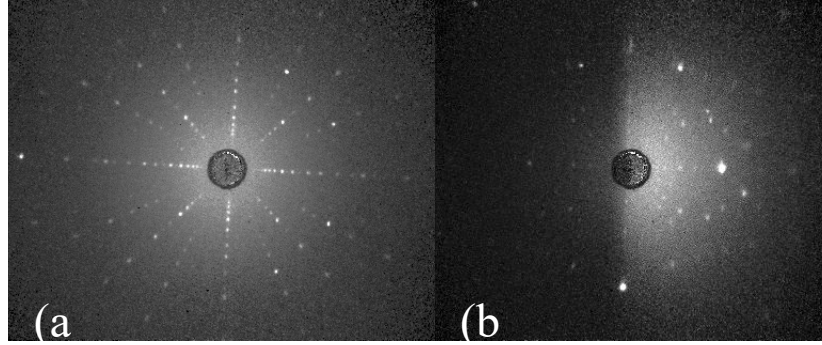In search of a possible pressure induced SC in CeCuAl$_3$, high pressure experiments were conducted with a focus on reaching highest pressure and lowest temperature at our disposal. The experimental conditions were significantly improved compared to previous attempts [31] (see section 3.3. CeCuAl3). The initial experiment was done employing hybrid-cylinder piston cell up to 3 GPa in a ^{3}He/^{4}He dilution refrigerator down to about 50 mK [12], since this pressure cell provides more flexibility in the experimental montage and is easier to use. Following efforts were focused on high pressure experiments in s-BAC pressure cells (see Figs. 10 and 11), which are considerably more challenging. Low temperature scans were measured employing a dry dilution refrigerator Triton 200 (down to about 8 mK) available at Slovak academy of sciences in Košice [38]. When attempting to reach low temperatures of mK range, it is important to bear in mind the effect of possible Joule heating of the measured sample. For this purpose, a measurement of the electrical current at lowest temperature was carried out with the use of magnetic flux noise thermometer [38]. First change in the temperature equilibrium at lowest temperature was detected at current value of approximately 140 μA. Utilizing these results, the excitation current of 50/80 μA was used for the measurement with larger/medium s-BAC to ensure a negligible Joule heating and a correct determination of the sample temperature. In order to correctly determine the pressure using lead manometer and to map overall temperature development of the electrical resistivity, the experiments at each pressure point were first conducted in a wide temperature range from room temperature to 4 K employing closed cycle refrigerator (CCR) [12].

Experiment in the hybrid-cylinder piston cell provided information in the region up to 3 GPa and down to 50 mK. No pressure induced SC was revealed in these experimental conditions. The residual resistivity of 20 μΩcm agrees well with the previous results [31], documenting a good quality of investigated sample. There were four attempts investigating $CeCuAl_3$ employing s-BAC, one for the largest cell (up to 6 GPa) and three for the medium cell (up to 12 GPa) (see section 2.3.1. Bridgman anvil cells). Two montages led to only poor results due to loss of electrical contacts on the sample during pressurizing the cells. Other two attempts were considerably more successful, one for each size of s-BAC.

Higher temperature experiments in CCR yielded the results on evolution of individual anomalies under applied pressure. An example of measured data is shown in Fig.33. Three anomalies were observed, i.e. lowest temperature anomaly connected to transition from paramagnetic to AFM state with a Néel temperature T_N, and two other anomalies previously attributed to Kondo effect influenced by CEF [30] (see section 3.3. CeCuAl3) at T_l (low temperature) and T_h (high temperature). Although a clear deviation from linear behaviour was observed at temperatures below 10 K, a characteristic kink at T_N could not be determined rigorously, since the data were limited to 4 K and above. Moreover, pressure redistribution in s-BACs is considerably worse in comparison to pressure cells with liquid PEM, which could result in a characteristic kink at T_N being smeared out and more difficult to distinguish. Nevertheless, a slight increase of T_N with applied pressure could be followed in agreement with previous results [31].
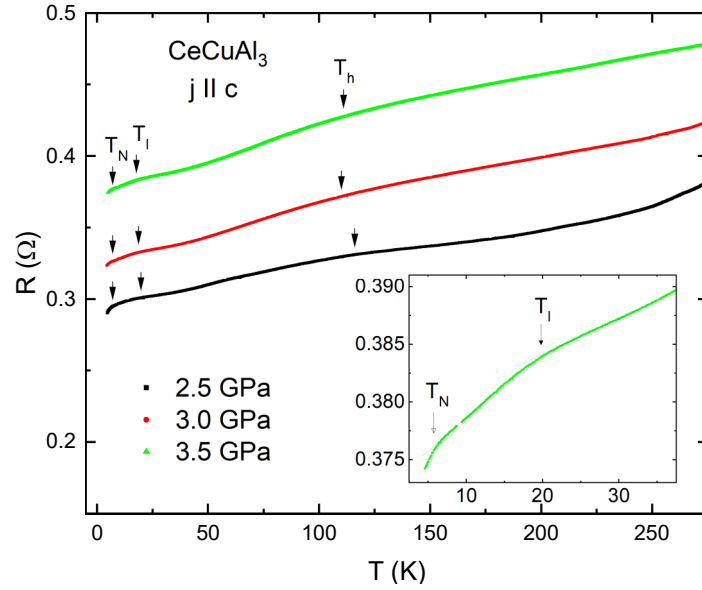
Fig.33: Electrical resistance of CeCuAl$_3$ as a function of temperature at various pressures. Experiment in the medium s-BAC pressure cell in CCR.

The anomaly at T$_l$ was determined as the onset of the kink in resistivity (a deviation of R(T) from linear behaviour as shown in the inset of Fig.33). The anomaly at T$_h$ was broad and therefore determined with intersection of 2 linear approximations of data above and below the kink. The pressure dependence of the individual anomalies from both experiments in s-BACs is summarized in a *T-p* phase diagram (Fig.34). The previously observed behaviour [31], i.e. the anomalies moving towards each other at higher pressures, finally merging at 8 GPa, was reproduced measuring the electrical resistivity employing larger s-BAC (full symbols in Fig.34). The change of respective temperatures is, however, less pronounced in our data. In contrast, continuing the measurement up to higher pressures using medium s-BAC (open symbols in Fig.34) does not reveal significant evolution of neither anomaly. T$_l$ remains almost constant above 3 GPa, as well as T$_h$. Overall uncertainty of determination of T$_h$ and T$_l$ was relatively high. Further uncertainty emerged during the experiment at higher pressures (p > 3.5 GPa): The conducting wire on the sample was lost forcing us to measure simultaneously composite signal from sample and lead.
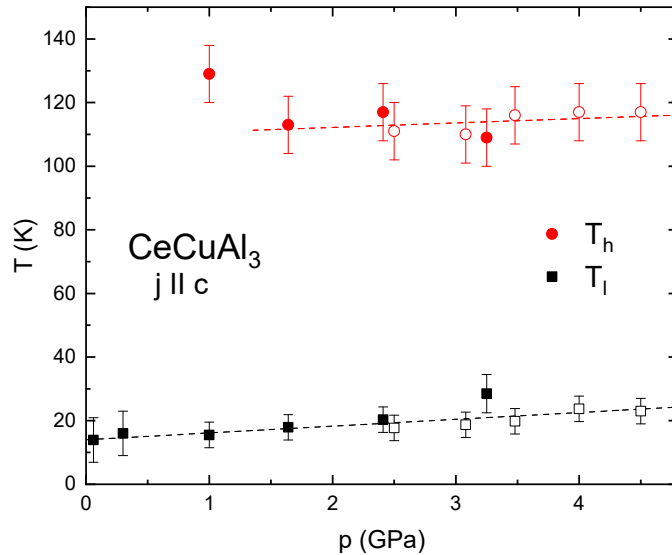
Fig.34: Pressure development of anomalies at T_h and T_l. Data from experiment with larger s-BAC (full symbols) and medium s-BAC (open symbols). T_h in low pressure region was not possible to determine as the contact wires were not well stabilized above 50 K (see 2.3.1. Bridgman anvil cells). Linear fits were performed for both sets of T_h (first pressure point unfitted) and T_l.

The electrical resistance was measured down to extremely low temperatures and high pressure (8 mK for 3.3 GPa pressure and 20 mK for other higher pressures) in the search for pressure induced SC. Up to external pressure of 4.5 GPa, no sign of SC transition was observed in CeCuAl$_3$ (see Fig.35). Since one conducting wire was lost between pressures 3.3 GPa and 4.3 GPa, a different part of sample was measured, varying the value of the electrical resistance. Therefore, all three curves shown in Fig.35 were scaled accordingly to present individual low temperature results (different R-axes for individual pressure data). Size of the sample and contact wires, together with the fact that they are not fixed to each other before pressurization (see Fig.10), make it difficult to correctly determine the structure factor necessary for the determination of resistivity values.
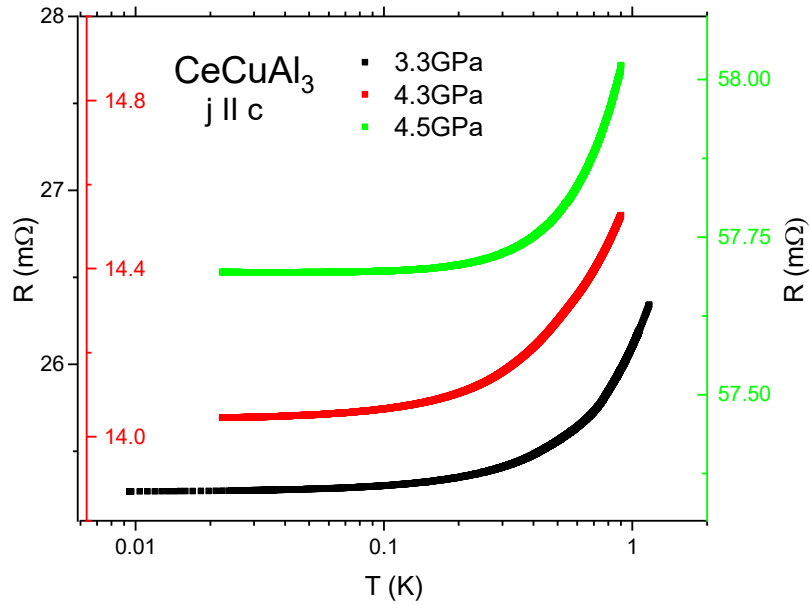
Fig.35: Electrical resistance of a CeCuAl$_3$ single crystal measured below 1 K and at various high pressures (smoothed and scaled data). The data at 3.3 GPa and 4.3 GPa were measured employing larger s-BAC, while medium s-BAC was used for measurement at 4.5 GPa.

4.3. Pressure exchange media calibration

To enhance the knowledge on sample environment conditions in the pressure cells, we decided to calibrate 3 liquid PEMa used typically in hybrid-cylinder piston cells and l-BACs (see section 2.3.3. High pressure media). To properly describe properties of these media, we performed a calibration experiment on each of them, focusing on their quality of hydrostaticity, magnitude of the pressure drop, *T-p* solidification points and compressibility. All experiments were conducted in a piston-cylinder type hybrid CuBe/NiCrAl pressure cell (see Fig.12) with the same experimental arrangement (see Fig.13). No strain gauges were used for calibration of the Daphne Oil 7373.

4.3.1. Hydrostaticity

In order to determine the hydrostaticity of PEM both during pressurization and temperature change, 3 manganin manometers were employed to determine pressure in different regions within the sample space. Using (14), pressure can be determined in-situ during the pressurization.

45

Fig.36 shows that Daphne Oil 7373, which is reported to solidify around 2.2 GPa at room temperature [16], behaves hydrostatically up to the solidification pressure. However, at higher pressures (in this cell up to 3 GPa) a large difference in pressures determined by individual manganin manometers (up to ~0.4 GPa), resulting from the non-hydrostatic behaviour of the solidified PEM, is observed. High pressure experiments in above listed types of pressure cells commonly use one manganin manometer situated in the place of manganin M1. Therefore, utilizing our results, pressure corrections should be applied in the pressure interval of solidified PEM in real experiment, depending on the respective positions of sample and manganin manometer.

Daphne Oils 7474 and 7575 which solidify well above 3 GPa (limit of used cell) [17,18] showed good hydrostatic conditions during the whole experiment. In Fig.36, Daphne Oil 7575 shows very small divergence of determined pressure (employing the three manometers) up to 3 GPa (during the pressurization at room temperature), where measured values match well for the three manganins within the experimental error of 0.05 GPa. Such observation was, however, not done inspecting the low-temperature data. The Daphne Oil 7575 low-temperature measurements showed a puzzling behaviour of hydrostaticity, resembling the solidification of Daphne Oil 7373 in similar pressure region. The unexpected development of the pressure drop (see following section) seems to be related to this behaviour.
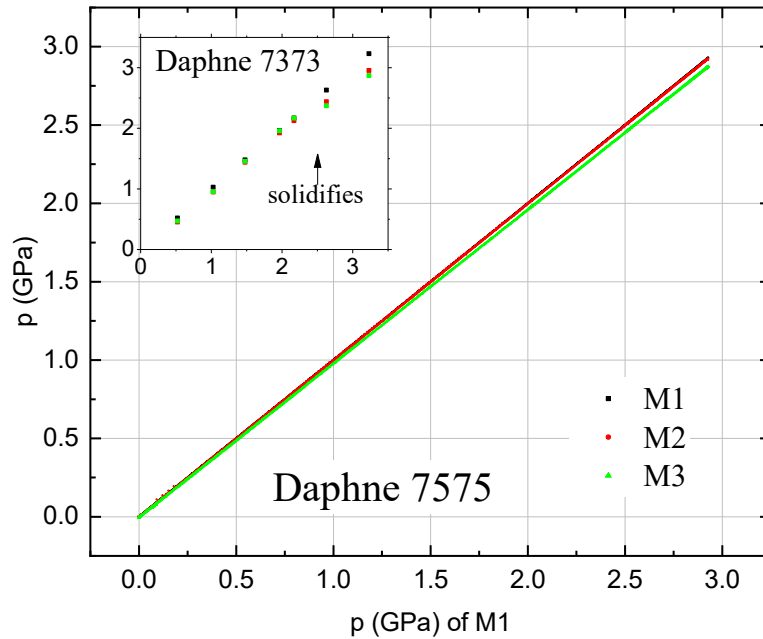
Fig.36: Pressure distribution within the sample space along the cell axis (manometers M1, M2 and M3) during the pressurization at room temperature. Pressure determined with M1 is used as a reference, in order to follow any deviation of pressures measured by M2 and M3 from M1.

Manganin manometers can be used to determine the pressure also at temperature lower than room temperature, nevertheless such an effort is accompanied by higher uncertainty, especially at very low temperatures. An approximate pressure change during the cooling/heating process can be thus evaluated. In this notion, we hoped to see the solidification of PEM during the cooling (from the resistance change of manganins), which proved unsuccessful in the end (leading to the use of SGs). On the other hand, we were able to observe that hydrostatic conditions remained in the whole sample space during the cooling down to about 4 K even when the PEM was long solidified. Therefore, the solidification induced by temperature variation is influencing the hydrostaticity significantly less than the solidification resulting from the pressure application at room temperature.

4.3.2. Pressure drop

High pressure experiments are often combined with low temperature measurements. Cooling the pressure cell down to low temperature is typically accompanied by the characteristic "pressure drop", i.e. the decrease in pressure caused mainly by thermal compression of PEM, as well as sample space components, and the material of the

pressure cell itself. The pressure at low temperatures can be determined employing the lead manometer, although its use is often experimentally challenging and restricting for other components of the sample space. Therefore, it is highly advantageous to utilize a known behaviour of the pressure drop of used PEM for pressure corrections of (from room to low temperature) manganin manometer. Pressure drop was calculated simply as the difference between pressures determined at room temperature using manganin manometer and at low temperatures utilizing lead SC transition (see Fig.37).
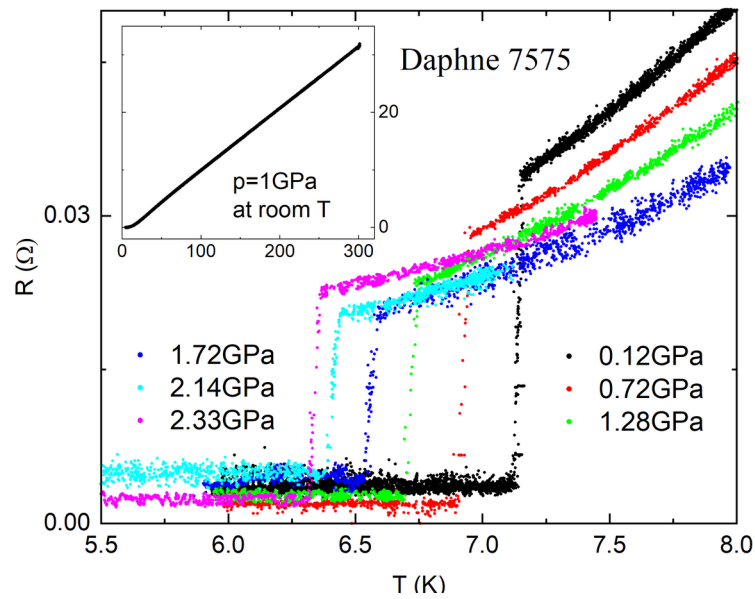
Fig.37: Determination of pressure at low temperatures utilizing the SC transition of lead (7.19 K at ambient pressure).

Results for the Daphne Oil 7373 show an approximately constant pressure drop of about 0.2 GPa in the liquid region up to 2.2 GPa (see Fig.38). Once it solidifies, pressures from different manganins start to deviate and the pressure drop increases significantly, namely for the manganin closest to the plug (M1). Interestingly, highest pressure in the solidified state is always measured closest to the plug and the lowest values on the other end of the sample space, i.e. close to the piston (M3).

Pressure drop measured in Daphne Oil 7575 is only slightly larger than that in Daphne Oil 7373, with a value of about 0.3 GPa. However, unexpected behaviour was observed at pressures around 2 GPa - the pressure drop had a tendency to

increase for higher pressures. Interestingly, such behaviour is similar to that of Daphne Oil 7373 at 2.2 GPa, where the solidification of this PEM occurs.

As there was single lead manometer to reveal the pressure at low temperature, while three manganin manometers were used for pressure determination at room temperature, a pressure drop can be determined accurately only for manganin manometer/position M2. The pressure drops determined for M1 and M3 provide us with rather qualitative values. A strong deviation of pressure drop values among the individual manometers is followed especially under non-hydrostatic conditions, most visibly for manganin M1 closest to the plug. Daphne Oil 7575 behaved hydrostatically in room temperature experiment. However, at low temperature (measured multiple times during the experiment), unusually large non-hydrostaticity was observed, resulting in notable increase of pressure drop value above 2 GPa.
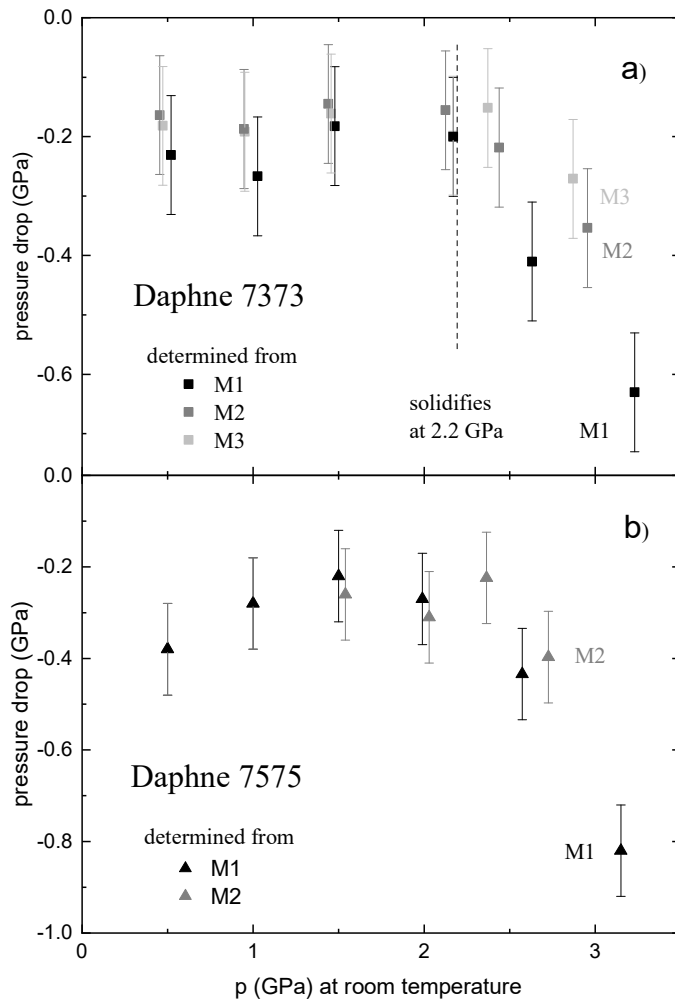

Fig.38: Pressure drop in Daphne Oils a) 7373 and b) 7575 determined from individual manganin manometers.

4.3.3. Solidification

Knowing the solidification temperature/pressure, i.e. the phase diagram of individual PEM is crucial for the understanding of hydrostatic/non-hydrostatic conditions during high pressure experiments. So far, solidification was studied mainly at room temperature or higher temperatures. Only a few solidification points were measured for Daphne Oil 7373 with the use of InSb manometer at lower temperature [39]. As was already mentioned, we were not able to observe solidification based on resistance behaviour of manganin manometers, therefore miniature strain gauges were employed in our experiments. It is shown in Fig.39 that the solidification of PEM manifests itself as an anomaly in resistance data of a SG. Increasing pressure shifts the anomaly towards higher temperatures, eventually to the room temperature at about 3.95 GPa [18].

Although, the principle of how SGs work is described with (15), to correctly determine strain, additional corrections on pressure change and temperature change must be included (such as the thermal/pressure change of resistivity of the grid alloy) [22,40]. Therefore, a positive change in the resistance of a SG with decreasing temperature observed in the liquid PEM does not necessarily mean the expansion of the SG.
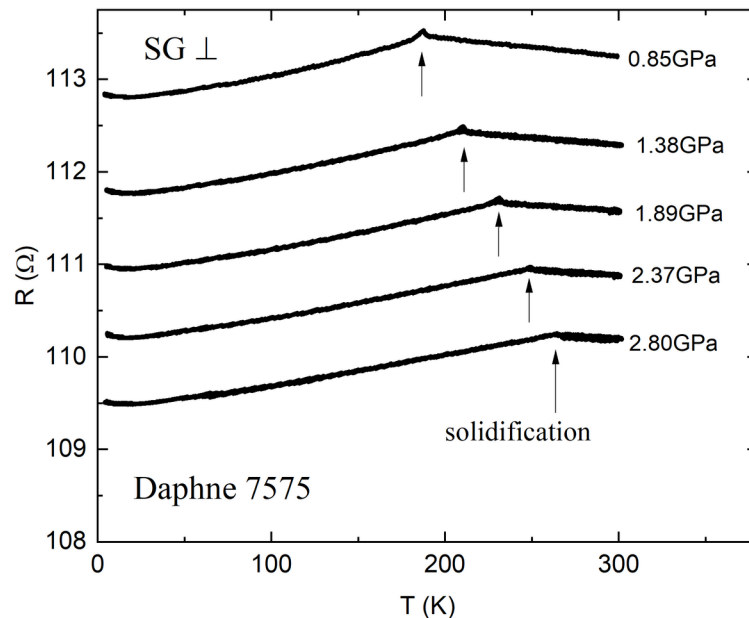

Fig.39: Temperature dependencies of the electrical resistance of SG $\perp$ (perpendicular to the axis of the cell). Anomalies in resistance represent the solidification temperatures.

The temperature dependencies of the resistance (of both SGs) reveal the same solidification temperature and a similar overall behaviour (see Fig.40,), but differ mostly in the solidification anomaly itself. During the cooling, both SGs exhibit similar behaviour – the anomaly is pronounced as a maximum in the resistance. During the heating, a large hysteresis is followed in the resistance of SG ‖, while only minor difference is observed in SG ⊥ data. Moreover, the anomalies corresponding to the PEM melting process exhibit significant jumps in the resistance, most interestingly a negative jump for SG ‖. Solidification points were determined as the local maxima/minima of the anomalies.
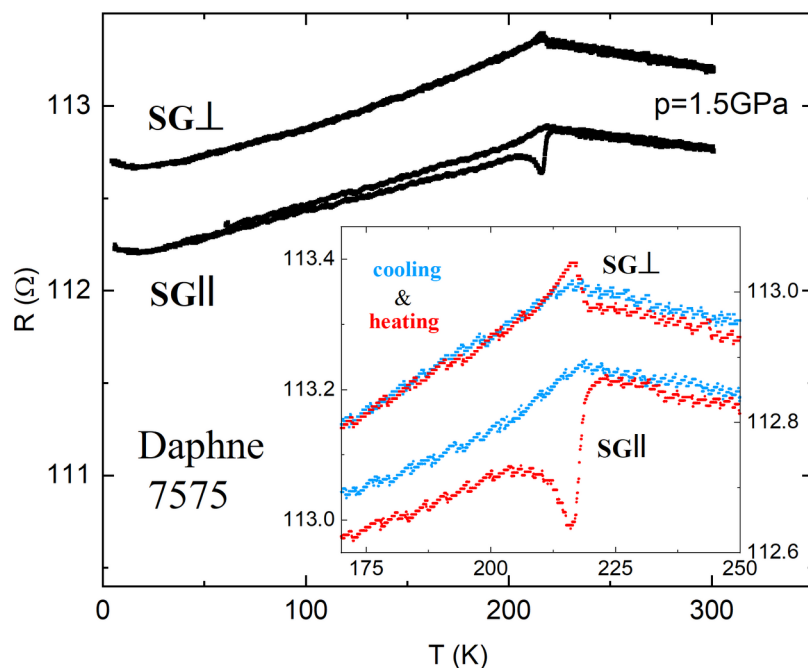
Fig.40: Difference in solidification anomalies between two SGs. The inset is a rescaled zoomed-in image for detailed illustration.

Determining the solidification points, T-p phase diagram was created to illustrate the border between solid and liquid state of individual PEMa (see Fig.41). A clear shift of the solid-liquid border to higher pressures with new generations of the Daphne Oils is demonstrated. Previously published data on Daphne Oils 7373 and 7474 assumed a linear behaviour of the border; only one point was known for Daphne Oil 7575. Adding our experimental points for Daphne Oils 7474 and 7575 measured below room temperature, we conclude that a linear approximation is not sufficient to describe the behaviour of investigated PEMa. Instead, a quadratic polynomial extrapolation can be used to characterize the solid-liquid border of the

two newest liquid PEMa. For Daphne Oil 7474, the resulting extrapolation can be written as

$$T_s(K) = 156.7 + 48.3\, p\,(GPa) - 2.4\, p^2\,(GPa^2)\,, \qquad (16)$$

and for Daphne Oil 7575 as

$$T_s(K) = 143.4 + 54.4\, p\,(GPa) - 4.1\, p^2\,(GPa^2). \qquad (17)$$
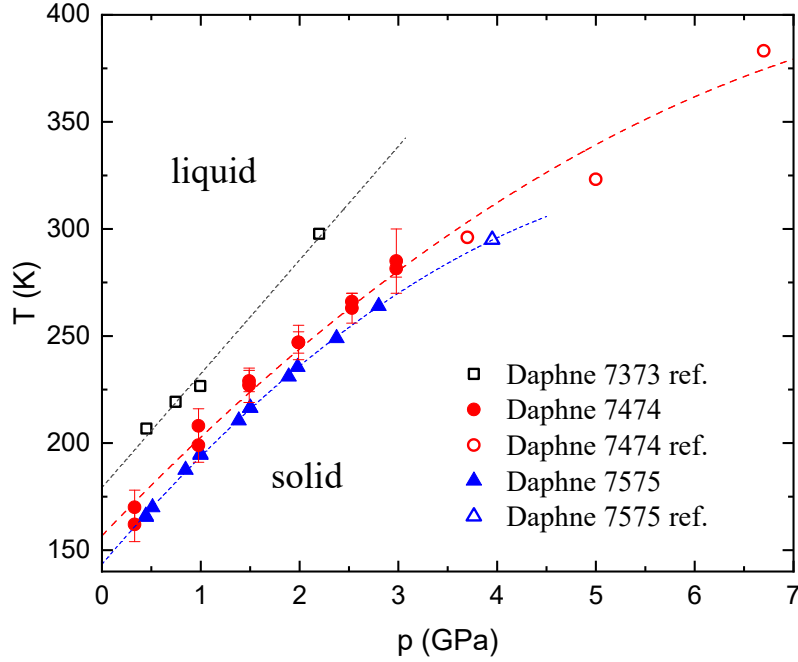
Fig.41: *T-p* phase diagram of three studied Daphne Oils. Data on Daphne 7373 [16] extrapolated linearly and data on Daphne 7474 [17] and Daphne 7575 [18] together with our experimental data extrapolated quadratically (16) and (17).

4.3.4. Compressibility

Ideally, liquid and solid PEM should be perfectly non-compressible. In reality, of course, liquids tend to compress significantly under high pressures of the magnitude used typically in high pressure experiments. Achieving higher pressures is always a compromise in the size of the sample space, which should be ideally very small. Therefore the volume of the sample space is very precious and high compressibility of the PEM can significantly reduce it, resulting in a severe experimental limitations.

Measurement of the compressibility of PEM in a piston pressure cell is generally relatively straightforward; all that is followed is the displacement of the piston during the pressure application. However, appropriate corrections are needed in order to determine the compressibility accurately. One of these correction is the compression of the Teflon cell, which has approximately the same volume as the

sample space and thus cannot be ignored. Data of the Teflon compressibility from [17] were used for the calculation of this correction. Another issue is a correct determination of the initial displacement of the piston at ambient pressure (a position at which the compression should be zero). Closing the pressure cell, tightening its components, e.g. the piston, seal rings etc., complicates a precise determination of the zero value of the compression of the sample space. The initial displacement was therefore identified closing the pressure cell by hand, i.e. an initial load of no more than few dozens of kg. The volume of PEM is further affected by the number and volume of the sample space components, which are not perfectly non-compressible. Also for that reason, each montage of pressure cell can result in a slightly different compression of the sample space.

To accurately describe compressibility in real high pressure experiment, we present data on uniaxial compression of the sample space rather than the compressibility of the PEM itself. This way, it is easier to estimate the loss of volume of the sample space, which is to be considered during the experimental montage, for piston cells particularly. All three investigated PEM exhibit a similar compression in the limits of 3 GPa piston cell (see Fig.42). Our data are in agreement with previously studied compression of Daphne Oils 7373 and 7474 in [17]. Daphne Oil 7373 becomes less compressible after it solidifies at 2.2 GPa, compared to the other two oils which stay in liquid state throughout the experiment, retaining their compressibility up to 3 GPa. Daphne Oil 7575 remains slightly less compressible than its predecessors, which is certainly advantageous for the real pressure experiment.
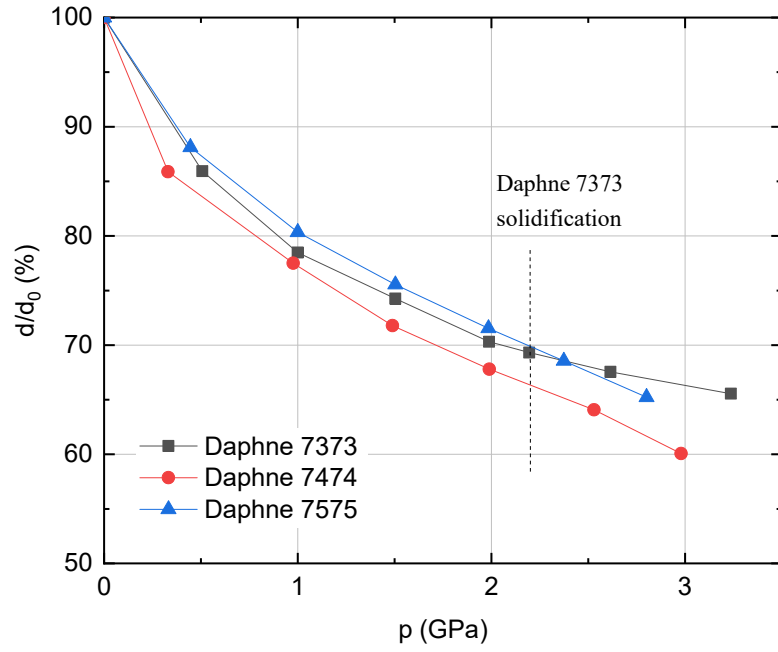
Fig.42: Uniaxial compression of the sample space along the axis of the cell for three studied PEMa from the Daphne Oil 7000 series.

5. Discussion

Firstly, let us discuss the results on $CeRhSi_3$. Single crystals can be prepared by both Czochralski and flux method. However, contrary to previous reports on $CeRhSi_3$ crystal growth [2,24,32], our attempts to prepare $CeRhSi_3$ by the Czochralki method were unsuccessful. Analysing the prepared ingots, multiple secondary phases was observed in X-ray diffraction patterns, although BSE and EDX techniques showed the sample surface being homogeneous. $CeRhSi_3$ single crystal investigated in present study was prepared by true-flux method using Sn as solvent. The size of prepared single crystals was small (Fig.22), but sufficient for high-pressure experiments. The shape of the crystals was more advantageous compared to Crochralski grown samples. Those samples are much larger and their orientation and adjustment for the experiment are connected to difficulties with proper orientation, ingot cutting, polishing, usually leading to a few degrees tilt out of desired crystallographic directions. With small flux samples grown along the principal crystallographic directions the uncertainty in sample orientation is significantly reduced.

The phase purity and correct stoichiometry of prepared single crystals was confirmed by EDX, and X-ray diffraction techniques (Fig.23) verified their tetragonal structure of $BaNiSn_3$-type. Even correct composition and structure do not ensure a desirable quality of the single crystal. Therefore, we measured specific heat and electrical resistivity on prepared samples and compared the obtained results to previously reported data [2,24,32]. A good quality of the crystal was documented by high RRR factor of 88. A sharp lambda anomaly in specific heat data and a kink on the electrical resistivity curve at $T_N = 1.6$ K were well in agreement with the antiferromagnetic phase transition previously reported for $CeRhSi_3$ [24,32].

Focusing on high-pressure results, a good agreement with previous results was followed. Initial increase of T_N with applied external pressure was confirmed. The characteristic kink at T_N was, however, influenced by the presence of pressure induced SC transition at lower temperature. Since the goal of presented study was to investigate SC dome at pressures above 3 GPa, only one pressure point was measured in the vicinity of SC emergence, i.e. 1.1 GPa. Comparing data in Fig.16 and Fig.26, it is evidenced that our data measured with electrical current applied

along the [110] crystallographic direction resemble more previous measurements along the a axis, rather than along the c axis [24]. Although we believe that the signs of the SC transition can be seen in 1.1 GPa data, the measurement to temperatures lower than 0.3 K would be necessary to unambiguously identify the SC transition. The measurement at 2.9 GPa perfectly matches with the previous data [2,24], showing a pronounced SC transition below 1.1 K and no sign of AFM transition.

Behaviour of pressure induced SC was investigated above 3 GPa in detail. T_c plateau between 2.5 and 3.0 GPa is followed by a suppression of SC transition to lower temperatures with further increase of external pressure (Figs. 27 and 28). Regrettably, the experiment was interrupted by broken bottom anvil before we could confirm a shift of SC transition below 0.3 K at 5 GPa. A complete disappearance of pressure induced SC between 5 and 6 GPa remains as the final conjecture. Without further data from higher pressures the possibility of unexpected behaviour, or the existence of another high pressure phase remains.

Magneto-resistance measurements on a $CeRhSi_3$ single crystal, with the magnetic field applied along the c axis, led to results consistent with previous lower-pressure experiments [2,24]. Moreover, a similar behaviour was observed in the Ir analogue [41]. The pressure induced SC observed in $CeIrSi_3$ is considerably more resilient to magnetic field applied along the c axis than along [110] direction, which is similar to the behaviour observed in $CeRhSi_3$. The huge critical field is very sensitive to pressure variation, as demonstrated in Fig.31. On this point, it would be interesting to investigate critical magnetic field applied along the c axis in pressures around 2.6 GPa, where it seems the pressure induced SC is at its finest. An investigation of both 2.6 GPa and highest pressure region (> 5 GPa) is planned in near future. We have already prepared the pressure cell with the second $CeRhSi_3$ single crystal.

Second part of the discussion is dedicated to the results on $CeCuAl_3$. Pressure dependence of electrical resistance in a wide temperature region provide us information on three anomalies at temperatures T_N, T_l and T_h, i.e. Néel temperature and two temperatures related to CEF scheme. Although initial pressure experiments indicated the behaviour reported in [31], i.e. T_l and T_h shifting towards each other with increasing pressure, overall results suggested only subtle dependence of T_l and T_h on pressure. The previous discovery of the, so called, vibron state in $CeCuAl_3$ led

to extensive study of its CEF parameters and eigen-energies, namely a dependence of CF scheme on chemical pressure was addressed in [35] (see Fig. 19). Inspecting the INS spectrum of $CeCuAl_3$, the energy scales of the first and second transitions coincide with the anomalies observed at T_l and T_h. From this viewpoint, the anomalies correspond to a believed magneto-elastic nature of vibron coupling [36], and are tied to electrons' deexcitations. Previous study [35] revealed a strong Cu-Al concentration dependence of excitation spectrum. The substitution of 5% of Al by Cu atoms led to a strong change of INS spectrum (Fig.19), shifting all the peaks by few tenths of meV ($\approx$ units of K). Focusing on the second excitation, the shift from approximately 9.8 meV to 7.5 meV (i.e. from 114 to 87 K) was observed [35]. This shift was ascribed to the change of lattice parameters by doping, the a and c parameters were decreased by doping by 0.25% and 1.5%, respectively. Also our previous study on the compressibility of $CeCuAl_3$ [22] showed the c-axis being significantly more compressible. Motivated by previous results on polycrystalline sample [31], where the two anomalies in electrical resistivity were getting closer with applied pressure, and INS results, we attempted to follow the same evolution of the two high-temperature anomalies on the single crystal. The anomaly at T_l shifts to higher temperature with applied pressure, however the increase of T_l is not pronounced as well as in polycrystalline study [31], compare Figs. 21 and 34. The highest temperature anomaly at T_h is influenced negligibly by applied pressure. At first T_h decreases, however at pressure above 1.5 GPa, no evolution is followed (The fitted dashed line in Fig.34 is almost constant.). The most interesting behaviour of anomalies at T_l and T_h was expected around 6-8 GPa [31]. Yet, high pressure techniques of employing s-BACs were without a doubt most challenging out of the three used pressure cell types, and did not allow us to measure up to such high pressure. Similar problem could stay behind our unsuccessful attempt to pressure induce SC in $CeCuAl_3$. Our experiment still continue though. We expected to utilize pressure as high as 12 GPa, which is the limit of the medium sized s-BAC (at least 10 GPa should be achievable). Working with s-BACs is however delicate and highly demanding on time and skills. Therefore a high respect grew towards all people successfully operating their pressure cell up to such high pressures. The other explanation behind no SC state in $CeCuAl_3$ could be find in a possible partial atomic disorder in the lattice. Compared to $CeRhSi_3$ reported to crystallize in the

BaNiSn$_3$-type structure [2,24,32], CeCuAl$_3$ was reported to adopt not only this non-centrosymmetric structure, but also other centrosymmetric (and therefore disordered) structure types (see Fig.14) [26,27]. A very recent NMR study of LaCuAl$_3$ revealed that the investigated sample contained besides the majority BaNiSn$_3$ phase, also the secondary phase described by other structure variants [28]. In other words, a partial disorder is present in the sample. On the other hand, NMR study of LaAuAl$_3$ with heavier Au atoms concluded the lattice to be of pure ordered BaNiSn$_3$-type. Assuming the crystal structure/disorder in Ce and La analogues is similar, it could prevent the pressure induced superconductivity in CeCuAl$_3$. NMR study on CeCuAl$_3$ is highly desirable to reveal its local structure, but challenging considering the magnetic moment of Ce^{3+} in the compound.

Comprehensive study of the basic properties of 3 PEMa from the Daphne Oil 7000 series gives insight into advantages/disadvantages of individual PEM performance and is to serve for pressure calibration in future experiments employing these oils. The most important property of PEM is the hydrostaticity tied to solidification. As shown in Fig.36, when the PEM is in the solid state during pressurization, the uncertainty of pressure determination greatly increases. More importantly, non-hydrostatic conditions can affect systems sensitive to pressure. In this regard, Daphne Oils 7474 and 7575 possess great advantage over Daphne Oil 7373 which solidifies at 2.2 GPa, since hybrid-cylinder piston cells with maximal pressure of 3 GPa are commonplace in the high pressure scientific community nowadays. Moreover, Daphne Oil 7575 pushes the solid-liquid border to even higher pressures than Daphne Oil 7474, which provides a room for the future advancements in hydrostatic piston-type pressure cells.

Inspecting the pressure drop (see Fig.38), certainly a smaller pressure drop is more advantageous for PEMa, which in this case favours Daphne Oil 7373. It is known that Daphne Oil 7474, which is similar in composition to 7575, is less viscous than Daphne Oil 7373 [17]. Therefore, it is reasonable to assume the lower viscosity is accompanied by a greater pressure drop. During the experiment, all three PEMa solidify at low temperature, which was unambiguously confirmed by measurements with the SGs (Fig.39). Nonetheless, the resistivity measured with manganin manometers develops smoothly with temperature within the whole temperature range

58

(300 – 4 K). Therefore, all three studied PEMa are suitable for experiments at low temperatures.

Comparing the compressibilities, all studied oils exhibit very similar behaviour, i.e. the sample space is reduced by about 35-40% pressurizing the cell up to 3 GPa (Fig.42). Together with the fact that the initial space in the Teflon cell is 14 mm long, it is safe to prepare experimental montages up to approximately 8.5 mm long. Longer montages may result not only in non-hydrostatic conditions (discussed above), but also in a possible damage of the sample space components and to loss of conducting wires.

Taking into consideration investigated properties, the choice of PEM for the high pressure experiment is dependent on individual circumstances. Although Daphne Oils 7474 and 7575 exhibit higher solidification pressure, Daphne Oil 7373 has smaller pressure drop and lower viscosity (i.e. easier to handle, fill the sample space). Being also considerably less expensive, Daphne Oil 7373 is still to be preferred for high pressure experiments up to 2 GPa (e.g. in case of larger size hybrid-cylinder piston cell with inner diameter of 6 mm). Conducting the experiments up to 3 GPa, combined with temperature scans over a large temperature interval, Daphne Oil 7474 would be favoured over Daphne Oil 7575, which reveal an anomalous behaviour of the pressure drop as well as signs of non-hydrostaticity, at around 2 GPa (Fig.38). Lower compressibility and lower solidification temperature make Daphne 7575 a better choice for higher pressure experiments, especially in higher temperature region.

Conclusions

Presented thesis was focused on two intermetallic compounds, $CeRhSi_3$ and $CeCuAl_3$, more specifically on their transport properties under high external pressure. Additionally, a calibration study of 3 liquid pressure exchange media from Daphne Oil 7000 series, frequently used in high pressure experiments, was conducted.

The preparation and characterization of a $CeRhSi_3$ single crystal was followed by the measurements of electrical resistivity performed under extreme conditions: low temperature, high magnetic field and high hydrostatic pressure. The presence of the pressure induced superconductivity was confirmed at pressure > 1.1 GPa and newly studied up to 4.6 GPa. Above 3 GPa, the suppression of superconducting transition to lower temperatures was observed. A characteristic superconductivity dome was estimated to close between 5 and 6 GPa. Applying the magnetic field on the sample shifted the SC transition to lower temperature. A high upper critical field of 13 T at 2.9 GPa was significantly suppressed increasing the pressure above 3 GPa. The *T-p* and *H-p* phase diagrams were constructed for pressure induced superconductivity in $CeRhSi_3$.

Transport properties of $CeCuAl_3$ single crystal were investigated at extremely low temperatures and high quasi-hydrostatic pressures. Pressure dependence of three anomalies at T_N, T_l and T_h were investigated in a wide temperature region. Only a moderate/subtle dependence of the anomalies on pressure was observed and discussed in the frame of crystal field excitations, specially so-called vibron state. No signs of pressure induced superconductivity in $CeCuAl_3$ were observed up to 4.5 GPa and down to 8 mK.

A detailed study of fundamental properties of three liquid pressure exchange media from Daphne Oil 7000 series, including measurements of hydrostaticity, solidification, pressure drop and compressibility, was conducted. Solidification properties of the media were illustrated in *T-p* phase diagram alongside comprehensive implications of medium's solidification on its hydrostaticity. The advantages/disadvantages of individual PEMa were discussed with respect to their usage for high pressure experiments in specific pressure and temperature ranges.

Bibliography

[1] P. Haen, P. Lejay, B. Chevalier, B. Lloret, J. Etourneau, M. Sera, J. Less-Common Met. 110, 321-325 (1985)

[2] N. Kimura, K. Ito, K. Saitoh, Y. Umeda, H. Aoki, Phys. Rev. Lett. 95, 247004 (2005)

[3] I. Sugitani, Y. Okuda, H. Shishido, T. Yamada, A. Thamizhavel, E. Yamamoto, T. D. Matsuda, Y. Haga, T. Takeuchi, R. Settai, Y. Onuki, J. Phys. Soc. Jpn. 75, 043703 (2006)

[4] D. T. Adroja, A. del Moral, C. de la Fuente, A. Fraile, E. A. Goremychkin, J.W. Taylor, A. D. Hillier, F. Fernandez-Alonso, Phys. Rev. Lett. 108, 216402 (2012)

[5] K. V. Samokhin, E. S. Zijlstra, S. K. Bose, Phys. Rev. B 69, 094514 (2004)

[6] Z. Arnold, High pressure in basic and material science, Institute of Physics AS CR, Na Slovance 2, 182 21 Prague 8, Czech Republic

[7] M. Eremets, High pressure experimental methods, Oxford University Press (1996)

[8] Ch. Kittel, Introduction to solid state physics, 8th edition, John Wiley & Sons (1985)

[9] J. M. Ziman, Electrons and Phonons: The Theory of Transport Phenomena in Solids, Clarendon press, Oxford (2001)

[10] E. Gratz, M. J. Zuckermann, J. Magn. Magn. Mat. 29, 181-191 (1982)

[11] B. Lorenz, C. W. Chu, Frontiers in Superconducting Materials pp 459-497, Springer, Berlin, Heidelberg (2005)

[12] webpage of MGML (Material Growth and Measurement Laboratory) https://mgml.eu/

[13] V.Valvoda, M. Polcárová, P. Lukáč, Zaklady strukturní analýzy, Karolinum, UK Praha (1992)

[14] J. Rodriguez-Carvajal, Physica B 192, 55 (1993)

[15] N. Fujiwara, T. Matsumoto, K. Nakazawab, A. Hisada, Y. Uwatoko, Rev. Sci. Instrum. 78, 073905 (2007)

[16] K. Yokogawa, K. Murata, H. Yoshino, S. Aoyama, Jpn. J. Appl. Phys. 46, 3636-3639 (2007)

[17] K. Murata, K. Yokogawa, H. Yoshino, S. Klotz, P. Munsch, A. Irizawa, M. Nishiyama, K. Iizuka, T. Nanba, T. Okada, Y. Shiraga, S. Aoyama, Rev. Sci. Instrum. 79, 085101 (2008)

[18] Idemitsu Kosan Co.Ltd., Daphne Oil 7575 Data sheet

[19] L. H. Dmowski, E. Litwin-Staszewska, Meas. Sci. Technol. 10, 343-347 (1999)

[20] B. Bireckoven, J. Wittig, J. Phys. E: Sci. Instrum. 21 841 (1988)

[21] M. S. Torikachvili, S. K. Kim, E. Colombier, S. L. Buďko, P. C. Canfield, Rev. Sci. Instrum. 86, 123904 (2015)

[22] D. Staško, Compressibility of an intermetallic compound, bachelor thesis, MFF UK, Prague (2018)

[23] K. H. Bennemann, J. B. Ketterson, Superconductivity: Volume 1: Conventional and Unconventional Superconductors, Springer-Verlag Berlin Heidelberg (2008)

[24] N. Kimura. Y. Muro, H. Aoki, J. Phys. Soc. Jpn. 76, 051010 (2007)

[25] M. Klicpera, P. Javorský, P. Čermák, A. Rudajevová, S. Daniš, T. Brunátová, I. Císařová, Intermetallics 46, 126-130 (2014)

[26] O. S. Zarechnyuk, P. L. Kripyakevich, E.L. Gladyshevskii, Sov. Phys. Crystallogr. 9,706 (1965)

[27] E. Bauer,N. Pillmayr, E. Gratz, G. Hilscher, D. Gignoux, D. Schmitt, Z. Physik B - Condensed Matter 67, 205–210 (1987)

[28] V. Chlan, P. Doležal, R. Sgallová, M. Klicpera, Ch. Franz, P. Javorský, J. Phys.: Condens. Matter 31, 385601 (2019)

[29] T. Nishioka, Y. Kawamura, R. Kobayashi, H. Kato, M. Matsumura, K. Kodama, N. K. Sato, J. Magn. Magn. Mater. 310 e12, (2007)

[30] Y. Kawamura, T. Nishioka, H. Kato, M. Matsumura1, K. Kodama, J. Phys.: Conf. Ser. 150 042088 (2009)

[31] Y. Kawamura, T. Nishioka, H. Kato, M. Matsumura, K. Matsubayashi, Y. Uwatoko, J. Phys.: Conf. Ser. 200 012082 (2010)

[32] Y. Muro, M. Ishikawa, K. Hirota, Z. Hiroi, N. Takeda, N. Kimura, H. Aoki, J. Phys. Soc. Jpn. 76, 033706 (2007)

[33] M. Klicpera, P. Javorský, P. Čermák, A. Schneidewind, B. Ouladdiaf, M. Diviš, Phys. Rev. B 91, 224419 (2015)

[34] S. Mock, C. Pfleiderer, H. v. Lohneysen, J. Low Temp. Phys. 115, 1-14 (1999)

[35] M. Klicpera, D. T. Adroja, K. Vlášková, M. Boehm, H. Mutka, B. Ouladdiaf, T. Guidi, P. Javorský, Inorg. Chem. 56, 12839-12847 (2017)

[36] P. Thalmeier, P Fulde, Phys. Rev. Lett. 49, 1588 (1982)

[37] M. Kontani N. Sugiharaa, K. Murase, N. Möri, Czech. J. Phys. 46 (S4) 2067 (1996)

[38] European Microkelvin Platform webpage – facilities of Slovak Academy of Sciences Košice, http://emplatform.eu/

[39] K. Murata, H. Yoshino, H. O. Yadav, Y. Honda, N. Shirakawa, Rev. Sci. Instrum. 68, 2490 (1997)

[40] J. Kamarád, K.V. Kamenev,Z. Arnold, Strain gage method of volume measurements under hydrostatic pressure, Institute of Physics, AS CR, Cukrovarnická 10, 162 00 Prague 6, Czech Republic

[41] R. Settai, Y. Miyauchi, T. Takeuchi, F. Lěvy, I. Sheikin, Y. Onuki, J. Phys. Soc. Jpn. 77, 073705 (2008)

List of Abbreviations

AFM – antiferromagnetic

BAC – Bridgman anvil cell

CCR – closed cycle refrigerator

CEF – crystal electric field

DAC – diamond anvil cell

DCMP - Department of Condensed Matter Physics

HF – heavy fermion

INS – inelastic neutron scattering

l-BAC – Bridgman anvil cell with liquid pressure medium

MGML – Material Growth and Measurement Laboratory

PEM(a) – pressure exchange medium/media

s-BAC – Bridgman anvil cell with solid pressure medium

SC – superconductivity/superconducting

SG – strain gauge

SO – spin-orbit (coupling)

PF – percentile filter (Origin software)

WC – tungsten carbide

α – pressure coefficient

$p = \frac{F}{S}$ – deviatoric stress tensor components

ε – strain

θ_D – Debye's temperature

λ – parameter describing the shape of the indenter

μ_0 – vacuum permeability

$\mu_0 H_c$ – critical field

ρ – resistivity

ρ_0 – residual resistivity contribution

ρ_{mag} – magnetic contribution to electrical resistivity

ρ_{phonon} – phonon contribution to electrical resistivity

σ – conductivity

$F\begin{vmatrix} H \\ H \end{vmatrix}$ – stress tensor

σ_{ij} – stress tensor components

τ – collision time

ω – phonon frequency

ω_D – average phonon frequency

$\vec{E}$ – electrical field

$\vec{J}$ – electrical current

a – radius of the contact area

C_p – specific heat

e - charge of an electron

F – force

F_H – Helmholtz free energy

G – strain gauge factor

H – magnetic intensity

$\hbar$ – reduced Planck constant

K – material constant

k_B – Boltzmann constant

m_e – mass of an electron

n – number of electrons per volume

$N(E_F)$ – electronic density of states at Fermi level

p – pressure

p_λ – pressure distribution of "dry" contact of two bodies

Q – applied load

r – position

R – resistance

r_m – relative resistance

S – area

T – temperature

t – time

T^* – additional anomalous temperature

T_c – critical temperature of superconducting transition

T_h, T_{Kh} – high anomalous temperature

T_l, T_{Kl} – low anomalous temperature

T_{mag} – magnetic ordering temperature

T_N – Néel temperature

T_S – solidification temperature

V – volume

V_{eff} – effective interaction between the electrons mediated by the electron-phonon coupling